

# Suppression of the vacuum space-charge effect in fs-photoemission by a retarding electrostatic front lens

Cite as: Rev. Sci. Instrum. **92**, 053703 (2021); <https://doi.org/10.1063/5.0046567>

Submitted: 04 February 2021 . Accepted: 04 April 2021 . Published Online: 06 May 2021

 G. Schönhense,  D. Kutnyakhov, F. Pressacco, et al.



View Online



Export Citation



CrossMark

## ARTICLES YOU MAY BE INTERESTED IN

[Time- and momentum-resolved photoemission studies using time-of-flight momentum microscopy at a free-electron laser](#)



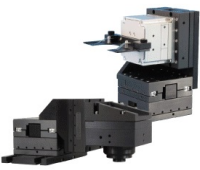
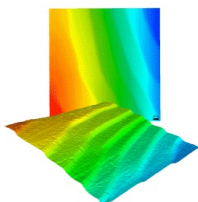
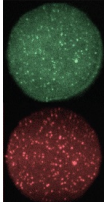
Review of Scientific Instruments **91**, 013109 (2020); <https://doi.org/10.1063/1.5118777>

[A quantitative comparison of time-of-flight momentum microscopes and hemispherical analyzers for time- and angle-resolved photoemission spectroscopy experiments](#)

Review of Scientific Instruments **91**, 123112 (2020); <https://doi.org/10.1063/5.0024493>

[Time- and angle-resolved photoemission spectroscopy of solids in the extreme ultraviolet at 500 kHz repetition rate](#)

Review of Scientific Instruments **90**, 023104 (2019); <https://doi.org/10.1063/1.5081938>

 <b>MCL</b> MAD CITY LABS INC. <a href="http://www.madcitylabs.com">www.madcitylabs.com</a>	<p>Nanopositioning Systems</p> 	<p>Modular Motion Control</p> 	<p>AFM and NSOM Instruments</p> 	<p>Single Molecule Microscopes</p> 
---	--	--	---	--

# Suppression of the vacuum space-charge effect in fs-photoemission by a retarding electrostatic front lens

Cite as: Rev. Sci. Instrum. 92, 053703 (2021); doi: 10.1063/5.0046567

Submitted: 4 February 2021 • Accepted: 4 April 2021 •

Published Online: 6 May 2021



G. Schönhense,<sup>1,a)</sup> D. Kutnyakhov,<sup>2</sup> F. Pressacco,<sup>2</sup> M. Heber,<sup>2</sup> N. Wind,<sup>3</sup> S. Y. Agustsson,<sup>1</sup> S. Babenkov,<sup>1</sup> D. Vasilyev,<sup>1</sup> O. Fedchenko,<sup>1</sup> S. Chernov,<sup>4</sup> L. Rettig,<sup>5</sup> B. Schönhense,<sup>6</sup> L. Wenthaus,<sup>2</sup> C. Brenner,<sup>2</sup> S. Dziarzhyski,<sup>2</sup> S. Palutke,<sup>2</sup> S. K. Mahatha,<sup>7</sup> N. Schirmel,<sup>2</sup> H. Redlin,<sup>2</sup> B. Manschwetus,<sup>2</sup> I. Hartl,<sup>2</sup> Yu. Matveyev,<sup>2</sup> A. Gloskovskii,<sup>2</sup> C. Schlueter,<sup>2</sup> V. Shokeen,<sup>8</sup> H. Duerr,<sup>8</sup> T. K. Allison,<sup>4</sup> M. Beye,<sup>2</sup> K. Rossnagel,<sup>7,9</sup> H. J. Elmers,<sup>1</sup> and K. Medjanik<sup>1</sup>

## AFFILIATIONS

<sup>1</sup>Johannes Gutenberg-Universität, Institut für Physik, D-55099 Mainz, Germany

<sup>2</sup>Deutsches Elektronen-Synchrotron DESY, D-22607 Hamburg, Germany

<sup>3</sup>University of Hamburg, Institut für Experimentalphysik, D-22761 Hamburg, Germany

<sup>4</sup>Departments of Chemistry and Physics, Stony Brook University, Stony Brook, New York 11790-3400, USA

<sup>5</sup>Fritz-Haber-Institut der Max-Planck-Gesellschaft, D-14195 Berlin, Germany

<sup>6</sup>Department of Bioengineering, Imperial College London, South Kensington Campus, London SW7 2AZ, United Kingdom

<sup>7</sup>Ruprecht Haensel Laboratory, Deutsches Elektronen-Synchrotron DESY, D-22607 Hamburg, Germany

<sup>8</sup>Department of Physics and Astronomy, Uppsala University, P.O. Box 516, 75120 Uppsala, Sweden

<sup>9</sup>Institut für Experimentelle und Angewandte Physik, Christian-Albrechts-Universität zu Kiel, D-24098 Kiel, Germany

<sup>a)</sup> Author to whom correspondence should be addressed: [schoenhe@uni-mainz.de](mailto:schoenhe@uni-mainz.de)

## ABSTRACT

The performance of time-resolved photoemission experiments at fs-pulsed photon sources is ultimately limited by the  $e$ - $e$  Coulomb interaction, downgrading energy and momentum resolution. Here, we present an approach to effectively suppress space-charge artifacts in momentum microscopes and photoemission microscopes. A retarding electrostatic field generated by a special objective lens repels slow electrons, retaining the k-image of the fast photoelectrons. The suppression of space-charge effects scales with the ratio of the photoelectron velocities of fast and slow electrons. Fields in the range from  $-20$  to  $-1100$  V/mm for  $E_{\text{kin}} = 100$  eV to 4 keV direct secondaries and pump-induced slow electrons back to the sample surface. Ray tracing simulations reveal that this happens within the first 40 to 3  $\mu\text{m}$  above the sample surface for  $E_{\text{kin}} = 100$  eV to 4 keV. An optimized front-lens design allows switching between the conventional accelerating and the new retarding mode. Time-resolved experiments at  $E_{\text{kin}} = 107$  eV using fs extreme ultraviolet probe pulses from the free-electron laser FLASH reveal that the width of the Fermi edge increases by just 30 meV at an incident pump fluence of  $22$  mJ/cm<sup>2</sup> (retarding field  $-21$  V/mm). For an accelerating field of  $+2$  kV/mm and a pump fluence of only  $5$  mJ/cm<sup>2</sup>, it increases by 0.5 eV (pump wavelength 1030 nm). At the given conditions, the suppression mode permits increasing the slow-electron yield by three to four orders of magnitude. The feasibility of the method at high energies is demonstrated without a pump beam at  $E_{\text{kin}} = 3830$  eV using hard x rays from the storage ring PETRA III. The approach opens up a previously inaccessible regime of pump fluences for photoemission experiments.

Published under license by AIP Publishing. <https://doi.org/10.1063/5.0046567>

## I. INTRODUCTION

Time- and angle-resolved photoelectron spectroscopy (tr-ARPES) using pump-and-probe techniques at the free-electron laser (FEL) or high-harmonic generation (HHG) sources is attracting rapidly growing interest. Time resolution in the range of some 10 fs provides new insights into challenging and fascinating problems such as charge order and charge-density-wave dynamics,<sup>1,2</sup> electron population dynamics and transient states,<sup>3–5</sup> or ultrafast phase transitions.<sup>6–9</sup> Soft and hard x-ray pulses from FELs give access to fs core-level dynamics<sup>7,10–12</sup> and allow “locking-in” to the coupled coherent lattice motion, exploiting photoelectron diffraction and x-ray standing waves.<sup>13–16</sup> The recent advances of full-field imaging momentum microscopes (MMs) have given a new drive to this rapidly developing field with extreme ultraviolet (XUV) or x-ray pulses from an FEL<sup>7–9,16–19</sup> or vacuum ultraviolet (VUV) pulses from HHG laboratory sources.<sup>20–24</sup> Emerging applications of tr-MM are ultrafast molecular orbital imaging<sup>19,25,26</sup> and the tracking of transient changes of topological properties and orbital textures of out-of-equilibrium states of matter.<sup>27,28</sup> Furthermore, full-field photoelectron diffraction is developing as a new powerful tool for structural analysis<sup>16</sup> as is demonstrated in first “static” experiments.<sup>29–31</sup>

The great potential of tr-ARPES/tr-MM is overshadowed by a serious obstacle, the Coulomb interaction of electrons confined in a small spatiotemporal phase-space volume. The performance of the experiments can be improved by pulse compression to gain higher time resolution, minimizing the size of the photon spot in order to reach better spatial resolution or increasing intensity for a better signal-to-noise ratio. However, all these attempts increase the Coulomb repulsion in the charge cloud. This dilemma is commonly referred to as the “vacuum space-charge problem.”<sup>10–12,32–36</sup> Space-charge interactions manifest themselves in shifts of kinetic energies and peak broadening, downgrading energy and angular/momentum resolution.

The situation is quite complex in pump–probe experiments because, on the one hand, the total amount of data needed is much higher than in “static” photoemission and, on the other hand, the mutual Coulomb interaction happens between several “species” of electrons, released by the pump and probe pulses at different times. Secondary electrons (SEs) and core-level electrons are emitted by the probe pulse at the same time as the photoelectrons of interest, while the pump-induced slow electrons are generally emitted at a different time than the primary electrons so that their forces on the photoelectrons depend on the pump–probe delay.<sup>12,17,37–39</sup> At XUV and x-ray energies, secondary electrons can outnumber the photoelectrons of interest by several orders of magnitude. The same is true for the pump-induced signal, especially in the strong pumping regime and/or if surface plasmon-polariton excitations (e.g., at structural inhomogeneities) are involved. Coulomb forces in the electron beam can cause serious artifacts in pump–probe experiments. In turn, the space-charge effects pose a limit to the total performance of tr-ARPES/tr-MM experiments. Until now, the only ways to cope with this inherent problem are to use sources with high pulse rates,<sup>40</sup> to avoid hot spots of strong plasmonic emission<sup>41</sup> in the field of view, or simply to reduce the pump and probe fluences until no significant shift and broadening occurs.

The Coulomb interaction in an  $N$ -electron system is *per se* strictly deterministic. However, photoemission is a stochastic

process, which shows up as “granularity” of the photocurrent. The deterministic interaction between a given photoelectron and the integral charge of all other electrons manifests itself in a rotation of the electron distribution in six-dimensional  $(\mathbf{r}, \mathbf{k})$  phase space. The stochastic contribution through individual  $e$ – $e$  scattering processes induces additional inhomogeneous broadening (irreversible “heating”) of the ensemble, visible in terms of energy broadening and randomization of the  $\mathbf{k}$ -distribution.<sup>42</sup> These effects are particularly serious for instruments comprising cathode lenses, such as photoemission electron microscopes (PEEM)<sup>43,44</sup> and MMs equipped with hemispherical analyzers<sup>45,46</sup> or time-of-flight (ToF) analyzers.<sup>47</sup> The strong accelerating extractor field of typically several kV/mm at the sample surface has a high collection efficiency for photoelectrons but also for the unwanted slow electrons. Anisotropic forces along the electron path in a cathode lens cause a Lorentzian-shaped deformation of the photoelectrons’  $E(\mathbf{k})$ -distribution.<sup>48</sup> A correction algorithm can eliminate the deterministic shift, but energy broadening and smearing of the  $\mathbf{k}$ -distribution remain (see also comment<sup>49</sup>).

The net result of all these considerations is that pump/probe experiments are typically run with significantly reduced sample current compared to “static” measurements done at synchrotrons. This is a serious problem because the measurement inherently requires orders of magnitude more data due to the dataset potentially gaining up to four additional dimensions due to the pump pulse, i.e., pump/probe delay, pump wavelength, pump polarization, and pump fluence.

Using a combination of ray tracing simulations and measurements at the free-electron laser FLASH and the storage ring PETRA III (both at DESY, Hamburg), we found a loophole out of this dilemma. The key ingredient is the fact that imaging electrostatic lenses in charged-particle optics can comprise both accelerating and retarding fields. By replacing the accelerating cathode lens with an extractor field by a strong retarding lens with short focal length right in front of the sample surface, the slow electrons can be rapidly removed from the photoelectron distribution. For an optimized lens geometry, all slow electrons with  $E_{\text{kin}} \leq 3$  eV are eliminated from the beam within the first 3, 15, or 150  $\mu\text{m}$  for retarding fields of 1000 V/mm (hard x-ray range), 200 V/mm (soft x-ray range), or 20 V/mm (XUV range), respectively. In addition, a saddle point in the retarding lens acts as a high-pass filter, confining the energy-width of the transmitted electron distribution. Experiments with fs XUV pulses at beamline PG2 (FLASH) and ps hard x-ray pulses at beamline P22 (PETRA III) validated that a specially tailored retarding front lens is a powerful means to eliminate a large fraction of the space-charge-induced energy shifts and broadening. A multi-mode lens allows switching between the retarding and accelerating modes. For comparison, we briefly address the literature results of the space-charge effect in conventional hemispherical analyzer setups.

## II. VACUUM SPACE-CHARGE EFFECTS IN PHOTOEMISSION WITH PULSED SOURCES

### A. Signatures of space-charge effects by secondary electrons and pump-induced electrons

Beyond a certain charge density in an electron beam, Coulomb forces can significantly influence the electron beam parameters. In

electron microscopy, this phenomenon is known as the Boersch effect.<sup>50</sup> Transversal forces deteriorate the lateral (momentum) resolution, and longitudinal forces broaden the energy distribution. The situation in photoemission with intense pulsed sources is different from the classical Boersch effect because several “species” of electrons interact with each other. Here, we summarize the essentials.

The measurements shown in Fig. 1 illustrate the three leading contributions to the space-charge problem encountered in tr-ARPES and tr-MM. These results have been recorded using the time-, momentum-, and spin-resolved ToF-MM setup (HEXTOF)<sup>17</sup> at FLASH in the conventional mode with an extractor at 8 kV. The first contribution is the force exerted by the cloud of *secondary electrons* (SEs) generated by cascade-like energy-loss processes inside of the solid. Figure 1(a) shows a wide-range photoelectron distribution  $I(E_{\text{kin}}, k_x, k_y)$  of a W(110) sample, recorded in 15 min at  $h\nu = 136$  eV. The ordinate scale is the time-of-flight, corresponding to a non-linear energy scale. The spectrum shows the valence band (VB, Fermi edge at  $E_{\text{kin}} = 130.5$  eV), the W 4f and 5p doublets ( $E_{\text{kin}} = 99.6/97.4$  eV and  $94.2/85.7$  eV, respectively), and the secondary electrons (SE). The  $E_{\text{kin}}$ -vs- $k_{\parallel}$  section and the spectrum reveal the high intensity of the SE cascade close to the bottom of the photoemission paraboloid. The upper part and the core-level patterns appear laterally contracted due to the chromatic aberration of the lens system.

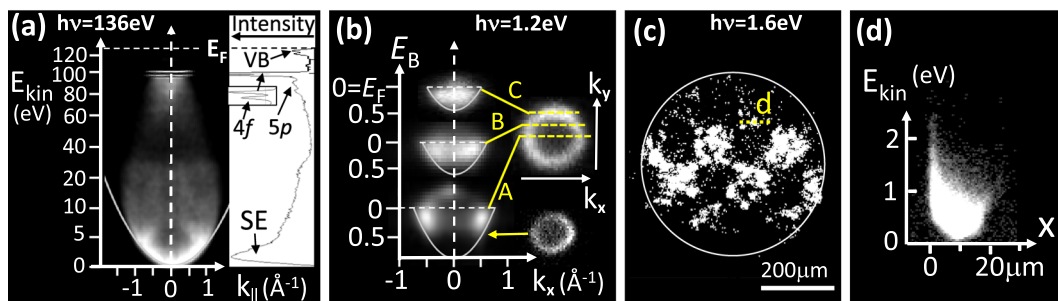
Even at this relatively low energy, the SEs significantly outnumber the electrons in the valence-band region of the spectrum. Their number rises strongly with increasing primary (photoelectron) energy. The energy and angular distribution of SE in the keV range has been studied and discussed in detail in the classical paper by Seiler.<sup>51</sup> The SE spectrum for metals has its maximum at  $\sim 2$  eV and has  $\sim 7$  eV FWHM, depending on the work function. For polycrystalline samples, where band structure effects and electron diffraction are averaged out, the angular distribution is a cosine function.

Figure 1(b) shows the analogous result for excitation by an infrared pump laser (80 fs, 1030 nm corresponding to  $h\nu = 1.2$  eV,

fluence  $5.6 \text{ mJ/cm}^2$ ). Given the work function of 5.5 eV, at least five photons are required to remove an electron via *multiphoton photoemission* (mPPE). The  $E_{\text{kin}}$ -vs- $k_{\parallel}$  section reveals a kinetic energy distribution up to  $>1$  eV with a pronounced space-charge-induced bulging of the top, as explained in Ref. 48. The bottom and center regions of the paraboloid appear dark, indicating saturation of the delay-line detector due to excessive count rates. Sections A, B, and C show, however, that the outer contour is paraboloid-shaped with a maximum diameter of a bit more than  $1 \text{ \AA}^{-1}$ , apparently somewhat widened by the Coulomb pressure in the dense distribution.

The third mechanism that can strongly contribute to space-charge artifacts is the so-called *plasmonic “hot spot” emission*.<sup>52–56</sup> Figures 1(c) and 1(d) show an example of a Au checkerboard pattern on Si at 800 nm ( $h\nu = 1.6$  eV). The real-space image in the PEEM mode (c) reveals strong emission from inhomogeneities in the Au squares. The horizontal stripe with two rows of squares represents the footprint of the pump beam (vertical width  $\sim 200 \mu\text{m}$ ). Figure 1(d) shows the energy profile across one of the hot spots [dashed line in (c)] and uncovers an inhomogeneous energy gain of up to  $\sim 2$  eV, being strongest at the outer rim of the structure, where the emission is maximum due to strong near fields<sup>57</sup> and possible additional ponderomotive forces contributing to the energy gain.<sup>58,59</sup>

This latter emission channel is a fingerprint of surface plasmon-polaritons in inhomogeneities acting as nanoantennas for infrared or visible radiation. The emission mechanism and its characteristic signature in space-charge effects are different from mPPE. Without going into detail, we recall that thermally assisted photoemission from a hot electron gas in a cluster, decay of a coherent plasmonic collective excitation into a single-electron excitation, or optical field emission can coexist, their interplay being governed by the Keldysh parameter; for details, see Refs. 57–60. In the following, we will term the electron signal from the pump pulse “mPPE” yield, keeping in mind that it may contain contributions from plasmonic emission.



**FIG. 1.** Photoemission measurements with the time-of-flight momentum microscope HEXTOF at FLASH, showing three sources of the space-charge effect. (a)  $E_{\text{kin}}$ -vs- $k_{\parallel}$  pattern and intensity spectrum of a W(110) sample excited with fs XUV-pulses from FLASH ( $h\nu = 136$  eV). The secondary electrons (SE) at the bottom of the photoemission paraboloid dominate the intensity spectrum. (b) Same but recorded with pump-laser excitation (1030 nm, fluence  $5.6 \text{ mJ/cm}^2$ ); sections A, B, and C correspond to different cuts through the  $k_x$ - $k_y$  pattern as denoted. (c) “Hot-spot” emission visible in a PEEM image taken at 800 nm, fluence  $2 \text{ mJ/cm}^2$  (checkerboard structure  $100 \times 100 \mu\text{m}^2$  Au squares on Si; Chessy test sample, Plano). (d) Line scan through one of the hot spots as marked in (c) revealing a structured kinetic energy distribution with maximum at the left rim (recorded close to normal emission).



## B. Cathode-lens type instruments—Time-resolved experiments using high extractor fields

In cathode-lens instruments (PEEMs, MMs), the sample is an integral part of the objective lens. The collection efficiency of the extractor field for low-energy electrons is very high. All slow electrons from a region  $>1$  mm on the sample surface are pulled into the lens system, as will be explained in Fig. 2(d). Hence, the slow electrons from the entire pump beam contribute to the space-charge shift, even if its footprint on the sample is large. The field aperture (FA), which confines the analyzed region, is located much further downstream in the microscope column. It thus cannot reduce the space-charge effect in this type of optics. When using this conventional accelerating lens mode (we term this *extractor-MM*) and operating with large pump fluences such that there are a large number of mPPE electrons, a small pump beam diameter is advantageous.

The slow electron cloud, confined by small transversal momenta and small energy spread, trails behind the fast photoelectrons and exerts long-range Coulomb forces. The pushing effect of the slow electrons with small  $k_{\parallel}$  is maximum along the optical axis and drops toward the rim of the k-field of view. The semi-analytical model in Ref. 48 predicts a Lorentzian deformation of the photoelectrons'  $E(k)$ -distribution. Fitting the measured deformation to the model allows correcting the deterministic part of the space-charge interaction. Xian *et al.*<sup>61</sup> gave a comprehensive overview of data treatment in pump-and-probe momentum microscopy, including *a posteriori* correction of the Lorentzian space-charge deformation and the related effect of spherical timing aberration.

Beyond the correction aspect, the measured shift allows quantifying the amount of charge in the slow-electron cloud. Energy shifts by the SE cloud are small in the VUV range (0.4 eV at 30 eV<sup>42</sup>) but increase strongly toward the soft x-ray range, where the number of SEs can exceed the number of photoelectrons by orders of magnitude. In valence-band photoemission from Ir(111) at  $E_{\text{kin}} \approx 1000$  eV, shifts up to 10 eV have been observed. The fit revealed a total charge of the SE cloud of  $\sim 10^6$  e/pulse, i.e., the number of SEs exceeds the number of fast valence-band photoelectrons by 4–5 orders of magnitude (see Figs. 1 and 2 in Ref. 48).

## C. Field-free photoemission—Time-resolved experiments using conventional analyzers

The signatures of the space-charge effects depend on the electron lenses and type of analyzer. In *conventional electron energy analyzers* [of hemispherical or angle-resolved ToF (ARTOF) type], the region between the sample and the entrance lens (typically 30–50 mm) is field free. Each electron “species” expands in its charge cloud, thereby steadily reducing the charge densities. Electrons emitted by a given pump or probe pulse undergo a “natural” separation according to their different velocities. Previous experimental results of field-free photoemission showed good agreement with model calculations for free-expanding photoelectrons and SE and mPPE charge clouds.<sup>10,12,36,37</sup> Here, we give an overview of existing results for different spectral regions, ranging from experiments at FELs in the hard x-ray range and XUV to HHG experiments in the VUV range.

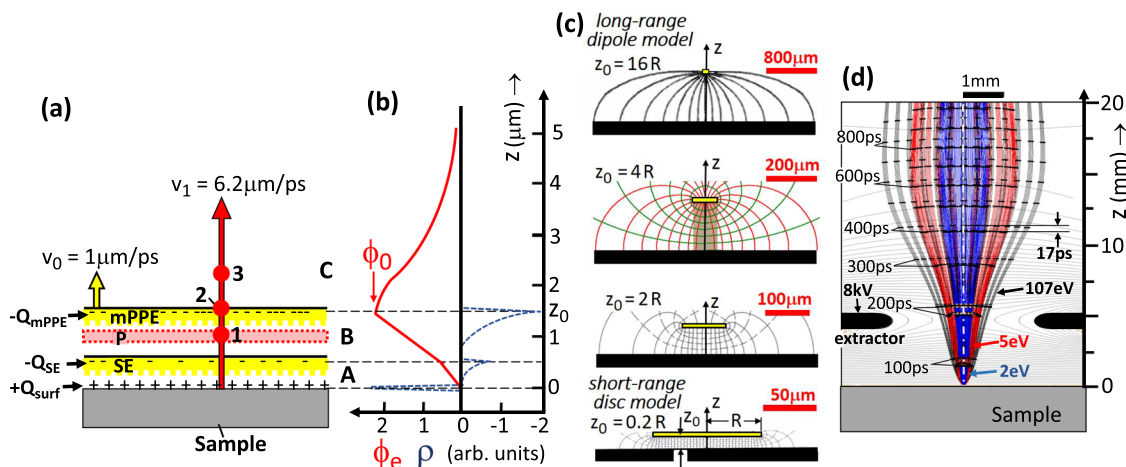


**FIG. 2.** Overview of short-range [(a) and (b)], intermediate-range (c), and long-range space-charge effects (d) in an *fs* pump-probe experiment: (a)–(c) without and (d) with lens fields. (a) Scheme of pump-induced multi-photon photoemission (mPPE), probe photoemission (P), and secondary electrons (SE) induced by the probe pulse; velocities correspond to  $E_{\text{kin}} = 3$  eV for mPPE and SE (yellow) and 107 eV for photoelectrons (red). The snapshot at  $t = 0.5$  ps after the probe pulse (for pump-probe delay  $\Delta t = 1$  ps) captures the essentials of the *short-range space-charge interaction*. (b) Dashed curve: idealized charge density  $\rho$  corresponding to the negative charge disks  $-Q_{\text{mPPE}}$  and  $-Q_{\text{SE}}$  (in regions A and B) and positive surface charge  $+Q_{\text{surf}}$ . Solid curve: potential energy of a probe electron  $\Phi_e(z)$  reflecting the charge disks as well as the dropping (dipole) field in region C. (c) Transition from the homogeneous field of a parallel-plate capacitor (bottom) to the dipole field of a point charge (top) with the increasing distance  $z_0$  (disk radius  $R$  identical in all snapshots). (d) Trajectory calculation elucidating the *long-range space-charge interaction* for the geometry of the HEXTOF momentum microscope [extractor +8 kV; photoelectrons  $E_{\text{kin}} = 107$  eV (black trajectories), accompanied by slow electrons (2 and 5 eV, marked in blue and red, respectively)]. Time markers (100 ps increment) illustrate the propagation of the three electron “species.” Fast and slow electrons (here emitted at the same time) travel for almost 500 ps at a constant time difference of  $\sim 17$  ps in the decelerating field region behind the extractor.

An early study of near-threshold photoemission using a hemispherical analyzer (Specs Phoibos 150) at high resolution ( $h\nu = 6$  eV, width 6 ps, spot size  $20\text{ }\mu\text{m}$ , no pump beam) revealed 2 meV shift and  $>10$  meV broadening already at 100 e/pulse.<sup>62</sup> The shift increases to 100 meV at 3500 e/pulse. Despite the “natural” increase in distance and reduction of charge density, measurements in the XUV range at FLASH ( $h\nu = 191$  eV) using a hemispherical analyzer (Scienta SES 2002) revealed a count-rate dependent Gaussian broadening of up to 2 eV and a comparable energy shift for the Ir 4f core-level signal. With an additional pump pulse ( $2.1\text{ mJ/cm}^2$  at 800 nm), the broadening increased to 2.5 eV (data from Hellmann *et al.*, cited in Ref. 42). The dependence on pump–probe delay was studied in the same setup for the Ta 4f core level at  $E_{\text{kin}} = 120$  eV at lower pump fluence (yielding  $\sim 4 \times 10^4$  mpPE e/pulse). The plot of the energy shift  $\Delta E$ -vs- $\Delta t$  reveals a sharp maximum of  $\Delta E = +150$  meV at  $\Delta t = 0$ , followed by a drop of the shift to half of its value at 300 ps and a tail that extends to  $>1$  ns (see Fig. 10 in Ref. 10). Toward negative delays, the energy shift drops more rapidly, reaching half of the maximum value already after  $\Delta t = -50$  ps. This asymmetric behavior of the pump-induced space charge originates from the difference in emission time of pump- and probe-induced electrons as well as their different velocities and screening behavior and will be addressed in more detail in Sec. III A.

Qualitatively similar effects were observed in the hard x-ray regime. Using a setup with a larger analyzer (Scienta R4000) at the XFEL SACLA (Japan), Oloff *et al.* studied the space-charge-induced shifts and broadenings for hard x-ray probe pulses ( $h\nu \approx 8$  keV).<sup>12</sup> For the Ti 1s core-level signal ( $E_{\text{kin}} = 3030$  eV), this experiment revealed a sharp maximum in the kinetic-energy shift of  $\Delta E = +3$  eV at  $\Delta t = 0$  and a drop to half of this value at 250 ps. The shift is still significant ( $\Delta E = +0.5$  eV) at  $\Delta t \approx 1$  ns (see Fig. 8 in Ref. 12). Although the electron velocity in this XFEL experiment is a factor of 5 larger than in the XUV experiment,<sup>10</sup> comparable or even larger space-charge effects are observed. However, the excitation level in this XFEL experiment was tremendous (500  $\mu\text{J}$ , pump-spot diameter 1.4 mm, i.e.,  $\sim 23\text{ mJ/cm}^2$ ), leading to a huge mpPE emission with up to  $>100$  eV kinetic energy.

Using a lab-based high-harmonics source in the VUV range ( $h\nu = 21.7$  eV), Maklar *et al.* compared the space-charge shifts and broadening between a hemispherical analyzer (SPECS Phoibos 150) and a low-energy ToF momentum microscope (SPECS METIS 1000) using the same setup with identical conditions of the sample ( $\text{WSe}_2$ ).<sup>63</sup> The authors observe a much larger influence of space charge in the MM compared to the hemisphere, underlining the necessity for developing effective countermeasures as presented in the present work. Using the hemispherical analyzer, they observe a shift of the valence bands of  $>50$  meV for a total number of probe-emitted electrons (photoelectrons and SE) of  $\sim 10^4$ ; the broadening has about the same amount. The mpPE-induced space-charge shifts (using 3.1 eV pump pulses) measured at fixed  $\Delta t = 0$  show a very similar dependence when plotted vs the number of pump-emitted electrons: for  $10^4$  mpPE electrons, the bands shift by  $\sim 100$  meV (Fig. 8 of Ref. 63). The same figure shows a strongly time-dependent, bipolar energy shift with an inflection point at  $\sim 4$  ps after pump–probe overlap, recorded with the MM, which is due to the “pump–probe matching condition” at these lower kinetic energies and which we will come back to in Sec. IV A again.

#### D. Very high repetition rates and high-pass filtering

The study<sup>63</sup> clearly shows the much stronger space-charge effect in the MM at such low energies as 17 eV since all electrons are pulled into the lens system by the positive extractor voltage, which can also be expected to be similarly valid for higher energies. Given a pump footprint of  $\sim 250\text{ }\mu\text{m}$  and a region of interest (ROI) of only  $20\text{ }\mu\text{m}$  (selected by the field aperture), the extractor field collects slow electrons from an area two orders of magnitude larger than the ROI. The authors of this study discuss the implications of this higher space-charge sensitivity of the *extractor-MM*, depending on the signal of interest in different pump–probe photoemission experiments. From this quantitative comparison, it becomes clear how strong the MM technique will benefit from the suppression of the main part of these space-charge effects, as discussed in Sec. III.

In addition to increased sensitivity to space charge, the MM technique can also potentially suffer a major limitation due to detector saturation. As currently conventionally operated, all electrons are collected and sent to a 2D time- and position-sensitive detector based on a microchannel plate (MCP) electron multiplier and a delay-line anode. These detectors can handle one (or a few with a segmented anode) electron per shot, and even with improvements in the anode, the MCP limits the total count rate to a few MHz. Thus, if the full photoelectron distribution, including secondaries, is incident on the detector, the signal rate for primary photoelectrons of interest must usually be drastically reduced. Put another way, the signal for the electrons of interest is limited not by the inherent signal size but by the attainable dynamic range of the detector with reasonable integration times. A hemispherical analyzer, by contrast, efficiently filters the electron distribution such that only electrons of interest are incident on the detector, and the dynamic range of the measurement is then more limited by the inherent signal size. In pump/probe measurements, the region of the photoelectron spectrum of interest is usually only a few eV near the Fermi level. Working at the 500 kHz repetition rate, Maklar *et al.*,<sup>63</sup> with the pump/probe conditions they explored and no high-pass filtering of the photoelectron distribution, found detector saturation to limit the signal size for this region of interest at a comparable number of photoelectrons per pulse as space charge, and this was a major factor in their conclusion that hemispherical analyzers can actually be superior for pump/probe measurements where the spectral region of interest is typically only a few eV near the Fermi level. For higher repetition rates,<sup>22,40,64</sup> the detector saturation issue becomes even more acute. Different strategies for highly parallelized recording are under development, either based on pixel-type architectures<sup>65,66</sup> or on stacks of many delay lines.<sup>67</sup>

Since the ROI is often the highest energy electrons emerging from the sample, the detector saturation problem can be mitigated to a large extent by high-pass filtering the electrons such that low-energy electrons do not reach the detector. This has recently been successfully used by Wallauer *et al.*<sup>26</sup> for high-performance pump–probe measurements using a retarding grid in front of the detector. However, the use of such grids can produce unwanted micro-lensing of the electron beam, which can deteriorate the image.<sup>68</sup>

As an alternative to a high-pass filter, a bandpass filter could be used to reduce the recorded electron spectrum. Such a bandpass is provided by adding a dispersive element to the ToF instrument.

An elaborate solution combines a hemisphere-based MM with a ToF detector.<sup>46</sup> This instrument allows ToF recording at 500 MHz pulse rates of synchrotron sources. A much simpler design employs a dispersive multipole element (asymmetric dodecapole) integrated into the straight ToF column.<sup>69</sup> The scheme presented in Sec. III has the advantage of solving both the space-charge problem and the detector saturation problem simultaneously.

### III. MODEL DESCRIPTION AND SPACE-CHARGE SUPPRESSION BY RETARDING FRONT LENS

#### A. Short-range space-charge interaction in pump-and-probe experiments

The strategy of space-charge suppression targets a short-range (tens of  $\mu\text{m}$ ) and a long-range regime ( $>10\text{ mm}$ ). On the short length scale, we describe the slow electron clouds as planar *mPPE* and *SE disks* moving in the  $z$ -direction. Their initial thicknesses depend on the pulse length and the mean free path of the slow electrons in the solid, typical values are few 100 nm. This value is small in relation to their diameter, given by the pump and probe photon footprints (typically 50–100  $\mu\text{m}$ ). The SE and mPPE electrons have kinetic energy distributions from 0 to  $\sim 5\text{ eV}$ . The corresponding velocity distribution starts at zero, and many electrons are in the range around  $v_0 = 0.6\text{ }\mu\text{m/ps}$  (1 eV) and less at 1.3  $\mu\text{m/ps}$  (5 eV). The “Coulomb pressure” in the clouds can lead to additional energy broadening and spatial spread in all directions. The primary photoelectrons escape from this region of high charge density with velocities between  $v_1 = 3$  and 30  $\mu\text{m/ps}$  for kinetic energies between  $E_{\text{kin}} = 25\text{ eV}$  and 2.5 keV.

Figure 2(a) shows a sketch of the electron distribution in front of a metallic surface in the case of “field-free” photoemission (no external fields); this figure is a modification of Fig. 1 in Ref. 37. The slow disks (marked in yellow) have long trailing wings because the  $E_{\text{kin}}$ -distributions reach to zero; their leading edges are less broadened. The charge density distribution  $\rho$  is schematically sketched as dashed curves in Fig. 2(b). The photoelectrons (P) can be valence-band or core-level electrons. Statistically, the distribution P is also located in a flat disk (marked in red) with much lower charge density compared to the SE and mPPE populations. For high-energy excitation, several core-level and valence-electron disks are present and interact with each other.<sup>35</sup> At our experimental conditions, the number of electrons in disk P is in the order of 1  $e/\text{pulse}$ . Hence, we can neglect the mutual Coulomb interaction between fast electrons.

The snapshot in Fig. 2(a) captures the charge distribution in front of the surface at  $t = 0.5\text{ ps}$  after the probe pulse for a pump–probe delay of  $\Delta t = 1\text{ ps}$ . We assume velocities of  $v_0 = 1\text{ }\mu\text{m/ps}$  (3 eV) and  $v_1 = 6.2\text{ }\mu\text{m/ps}$  (107 eV), corresponding to the experiments discussed in Sec. IV. The mPPE cloud is emitted 1 ps earlier than the other electrons, and, thus this disk has traveled already a distance of 1  $\mu\text{m}$  when the probe pulse arrives, and so the snapshot corresponds to  $z_0 = 1.5\text{ }\mu\text{m}$ . The fast photoelectrons (red arrow) are emitted at the same time as the SE cloud and overtake the mPPE cloud at some distance, depending on the relative velocities. We distinguish three regions between the sample surface and SE cloud (A), SE and mPPE clouds (B), and mPPE cloud and vacuum (C). Photoelectrons in region B (red dot 1) feel the net force from both disks,

which can be retarding or accelerating, depending on the charge densities.

The forces in the different regimes can be understood in terms of a parallel plate capacitor with different charges on the plates.<sup>70</sup> The “plus pole” is the thin carpet of positive charge [width of the “spike” of  $\rho$  exaggerated but maximum much higher than plotted in Fig. 2(b)] residing at the surface due to the Coulomb forces in electrostatic equilibrium. For a metallic surface, this charge is actually a lack of electron density in the “spill-out” region in front of the surface (see Fig. 3 in Ref. 71). In photoemission, the surface dipole constitutes the main contribution to the work function.<sup>72</sup> The free-electron charge disk defines the potential  $\Phi_0 = \Phi_e(z_0)$ , similar to a conventional capacitor.<sup>73</sup>

$\Phi_e(z)$  denotes the potential energy of a probe electron traveling along  $z$  [see Fig. 2(b)] with  $\Phi_e = 0$  inside of the sample. Analyzing the static situation of Figs. 2(a) and 2(b), we bear in mind that electrostatic forces are conservative such that changes in kinetic energy are given by the electrostatic potential  $\Phi_e(z)$ . Thus, the final kinetic energy ( $z \rightarrow \infty$ ) is not altered by the charge disks. However, the electric fields are time-dependent, lifting the energy-conservation law of electrostatics by inducing forces. With an increase in time, two effects happen: (i) In the regime of a parallel-plate capacitor with a homogeneous field, the potential difference between the “plates” increases linearly with the distance  $z_0$ . (ii) For  $z_0 > 2R$  ( $R$ , disk radius), the potential distribution evolves into a dipole potential, which drops with  $z^{-2}$  [see the sequence in Fig. 2(c)]. Note the different length scales indicated by the scale bars for a typical spot size of  $R = 50\text{ }\mu\text{m}$  and the strong spreading of the positive surface charge during this transition.

We consider the case of strong pump but weak probe fluence (i.e., negligible SE charge). When the photoelectron approaches the mPPE disk, it is retarded; simultaneously, the positively charged surface moves away from the disk with  $v_0 \sim 1\text{ }\mu\text{m/ps}$  [phase 1 in Fig. 2(a)]. After piercing through the charge cloud (instant 2), the photoelectron feels the accelerating Coulomb force from the disk (phase 3). Since the positive surface charge is steadily moving away from the disk, its screening effect is reduced, and hence, the net retardation (better-screened phase) is smaller than the net acceleration (less-screened phase). For realistic parameters [ $R = 50\text{ }\mu\text{m}$ ,  $z_0 = 1.5\text{ }\mu\text{m}$  (corresponding to  $t = 1\text{ ps}$ )], the capacitance of the mPPE disk and surface-charge carpet is 0.05 pF, yielding  $\Phi_e(1.5\text{ }\mu\text{m}) = -2\text{ V}$  for a realistic value of  $Q_{\text{mPPE}} = 100\text{ fC}$ . At  $t = 2\text{ ps}$ , the capacitance has dropped to 0.03 pF, yielding  $\Phi_e(2.5\text{ }\mu\text{m}) = -3.3\text{ V}$ , causing a sizable acceleration. With increasing time, the lateral and longitudinal spread of the charge disk becomes significant, and this simple capacitor model is no longer valid. The acceleration is stronger for *negative pump–probe delay*, where the retarding phase is missing and strongest for  $\Delta t = 0$ , because then the slow electrons are closest to the photoelectrons. Figures 2(a) and 2(b) represent a generalized version of the model described in Refs. 10, 12, 36, and 37, where more details of this complex scenario are given.

The *asymmetry in the retarding and accelerating phase due to the continuous dropping of the screening from the positive surface charge* is the essential mechanism of the space-charge acceleration effect close to the sample. We get further information from a simplified kinematic model exploiting the mirror-charge concept<sup>71</sup> (which formally introduces a potential inside of the metal). The superposition of a moving negative charge disk ( $-Q$ , radius  $R$ ) at a distance

$z_0 = v_0 t + \Delta z$  (with  $\Delta z = v_0 \Delta t > 0$ ) and a positive mirror-charge disk at  $-z_0$  moving in opposite direction leads, after integration of the force over the path of the photoelectron, to an *energy gain* of

$$W = -e\Phi_0 \frac{2\beta}{1-\beta^2} \left\{ \sqrt{1 + \left(\frac{\Delta z}{R}\right)^2} - \left|\frac{\Delta z}{R}\right| \right\}, \quad (1)$$

with the potential in the disk

$$\Phi_0 = \Phi(z_0) = \frac{1}{2\pi\epsilon_0} \frac{Q}{R} \quad (2)$$

and the slow-fast velocity ratio  $\beta = v_0/v_1$ . By assuming monoenergetic electrons in the disks and neglecting changes in kinetic energy and expansion of the disk, the model is strongly simplified. Its elegance lies in the fact that the entire dynamics is cast into a few parameters. Notably, the energy gain increases with  $\Phi_0$ ,  $\beta$ , and the ratio  $\Delta z/R$ . In reality, there is a continuous velocity distribution down to  $v_0 = 0$ , and the net acceleration is an integral over the different velocities, weighted by the corresponding number of electrons.

We conclude that for a given pump fluence, one can minimize the space-charge effect by the following two strategies:

- A decelerating field in front of the sample surface results in a decrease and finally reversal of  $v_0$ . In turn, the energy gain  $W$  will be smaller and drop more rapidly with increasing delay  $\Delta t$ .
- In this model, the reduction of  $R$  at constant pump fluence ( $Q \propto R^2$ ) leads to a proportional reduction of  $\Phi_0$  ( $\Phi_0 \propto R$ ). In addition, the dipole-like drop for large  $\Delta z/R$  is reached earlier. However, an inhomogeneous pump fluence in the ROI is detrimental, as will be discussed in Fig. 6(u).

## B. Long-range space-charge interaction in cathode-lens instruments

The *short-range space-charge interaction* discussed in Sec. III A causes spectral distortions very close to the surface ( $\mu\text{m}$ -range). In cathode-lens instruments (PEEMs and MMs), an additional *long-range space-charge interaction* appears. The accelerating field of the extractor electrode in the objective lens has a high collection efficiency not only for the photoelectrons but also for slow electrons. Using the same lens geometry and parameters like in the experiment at FLASH (extractor 8 kV;  $E_{\text{kin}} = 107$  eV for the photoelectrons), we simulated the time-dependent electron trajectories within the electron lens system of Fig. 2(d). The slow electrons (here launched at  $\Delta t = 0$ ) trail behind the photoelectrons as charge disks (blue and red for 2 and 5 eV, respectively), visible by the time markers. In the retarding-field range behind the extractor electrode, the fast and slow electrons approach each other again. Within a long time interval of 500 ps (corresponding to a path interval of 7 mm), the wave fronts of the 107 and 2/5 eV electrons travel in a small distance ( $<1$  mm), corresponding to a time difference of 17 ps. We conclude that for a pump-probe delay of 17 ps, the populations of *mPPE* electrons and fast photoelectrons travel very close to each other for a long time, giving rise to a significant integral Coulomb force. At larger time, the distance of the two “species” increases again. This is the essence of the *long-range space-charge interaction*, which does

not occur in field-free photoemission. Figure 2(d) summarizes the model described in detail in Ref. 48, where more details are discussed. The results of Fig. 2(d) agree quantitatively with experiment, as will be discussed in Sec. IV A [Fig. 5(e)].

*Stochastic scattering events* of type *slow e-fast e* happen when the photoelectrons cross the mPPE disk (red dot 2) in Fig. 2(a). Scattering might also occur for the “pump-probe matching condition,” here at  $\Delta t = 17$  ps. However, the charge density is strongly reduced due to the increased beam diameter at  $z = 14$  mm, which diminishes the scattering probability. Although the probability for such events scales with the integral charge, such binary *e-e* scattering processes should correctly not be termed the space-charge effect because they are not caused by the integral charge. Note that in *slow e-fast e* scattering events, the fast electron loses energy and drops out of the observed energy window, whereas the space-charge interaction of a slow macrocharge traveling behind a fast photoelectron is accelerating.

Here, we have ignored all kinds of inhomogeneities, e.g., due to the spatial pump and probe beam profiles and their overlap but also due to temporal fluctuations or the “granularity” of the photocurrent even for a perfectly homogeneous surface. This causes an inhomogeneous field distribution inside of the capacitors. The enhanced emissivity in hot spots [Figs. 1(c) and 1(d)] can locally enhance these inhomogeneities. In turn, the effective potential curve [Fig. 2(b)] will generally be smeared out, leading to laterally inhomogeneous decelerating or accelerating forces.

## C. Design of a low-aberration retarding field lens for space-charge suppression

The space-charge suppression mode makes use of a well-known general property of charged-particle optics: Imaging electrostatic lenses can be accelerating or retarding. Figure 3 shows a comparison of electron trajectories calculated for the retarding suppressor lens mode, in brief *repeller-MM* [(a)–(c)], and the accelerating conventional cathode lens mode, in brief *extractor-MM* [(d) and (e)]. The front lens is optimized for the repeller mode but works as well for the accelerating mode. The geometry of the lens group is identical in (a) and (c)–(e) and only the lens excitations (applied voltages) are different in cases (a) and (c), and (d) and (e).

The common understanding of a conventional PEEM or MM optics is that a strong extractor field is required to collect all photoelectrons from a large solid-angle interval. The strength and shape of the field is illustrated by the equipotential contours in Fig. 3(d). In terms of charged-particle optics, an accelerating cathode lens must be described as consisting of three components: (i) In the strong homogeneous accelerating field, the electrons travel on parabolic trajectories [see the ray bundle close to the sample in (d)]. The extractor field causes a virtual source image behind the sample, in twice the sample-extractor distance.<sup>44</sup> (ii) The anode bore is an aperture lens,<sup>50</sup> i.e., a purely diverging lens that shifts the virtual source image into the region close to the anode bore [dashed green line in (d)]. (iii) The subsequent lens elements (not shown in Fig. 3) convert this virtual image into a real image at the position of the *field aperture* in (e). A set of nine selectable apertures define the size and position of the ROI, independent of the size of the photon footprints. However, the field aperture cannot reduce the space-charge shift because this has happened already upstream of the aperture. A reciprocal



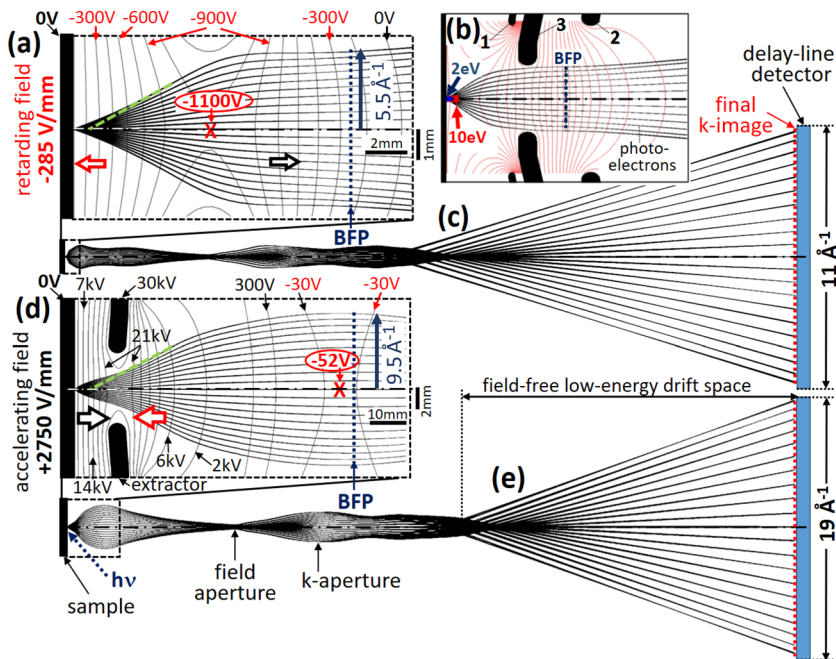


**FIG. 3.** Comparison of the space-charge suppression mode [(a)–(c)] and the conventional mode [(d) and (e)] of a new multimode objective lens; simulations for an initial kinetic energy of 1.5 keV. Equipotential contours are labeled by black and red numbers for the accelerating and retarding case, respectively. Detail (b) shows a result for a lens geometry with the steering electrode (data taken from Ref. 76). Note the striking similarity (apart from the length scale) of the trajectories for the retarding (a) and accelerating mode (d). Lens geometry identical for (a) and (c)–(e); only lens potentials and focal lengths are different (see scale bars). The saddle points [red crosses in (a) and (d)] yield different high-pass characteristics (see text). All trajectory calculations have been made using SIMION8.1.<sup>77</sup>

image (k-image) is located in the backfocal plane (BFP) [see dotted blue line in (d)]. A set of k-apertures, marked in (e), is located in the second k-image (conjugate plane of the BFP). It confines the diameter of the momentum range, e.g., for real-space imaging at high energies.

For the retarding mode [Fig. 3(a)], the electric field is an order of magnitude smaller and oppositely directed as in (d). Despite the strong retarding field of  $-285$  V/mm at the sample surface, the photoelectron trajectories look similar (apart from a different length scale, see scale bars) as in the accelerating case with  $+2750$  V/mm. This counter-intuitive result reflects the fact that a properly designed retarding lens field can be converging (convex lens). The initial diverging action of the retarding field is visible in the trajectories, but at the left  $-900$  V equipotential surface, an inflection point appears and the lens action becomes converging. The tangent to the trajectory at the inflection point [green dotted line in (a)] shows that a virtual source image exists on the optical axis, similar to the accelerating case (d). In order to maximize the retarding field, the focal length of the objective lens in (a) is shorter than in the accelerating case (d); the first electrode is just outside of figure (a) (see scale bars). A more flexible geometry including a steering electrode is shown in (b) (from Ref. 76).

We summarize the differences between the *repeller*-MM and *extractor*-MM modes, as simulated for identical electrode geometries but different lens voltages:

- The retarding field of  $-285$  V/mm in Fig. 3(a) decelerates the slow electrons until they reach a turning point and move back to the sample; electrons with  $E_{\text{kin}} \leq 3$  eV turn around within the first  $10 \mu\text{m}$ . Due to the strong acceleration in the *extractor*-MM (d), the fast and slow electron “species” stay closely together and interact over flight paths up to tens of mm.<sup>48</sup>

- The retarding field in (a) persists until a saddle point with potential  $-1.1$  kV at  $8$  mm from the surface, marked by a red cross. This saddle point acts like a high-pass filter, which in the present example removes all electrons with  $E_{\text{kin}} < 1.1$  keV (including electrons from intense core-level transitions) from the beam. In the accelerating case (d), there is only a weak saddle point of  $-52$  V close to the BFP.
- The larger angular filling factor of the retarding lens shows up in a reduction of the maximum usable k-field of view. For the simulated example, the diameter is  $11 \text{ \AA}^{-1}$  in the retarding case (a) instead of  $19 \text{ \AA}^{-1}$  in the accelerating case (d).
- The usable energy interval in the ToF k-microscope in the suppressor mode is smaller by a factor of 2 to 3 due to the larger chromatic aberration of the retarding lens.

This design study targets fs-sources in the XUV and soft x-ray range. The simulations in Fig. 3 have been performed for  $E_{\text{kin}} = 1.5$  keV and a high-energy MM optics similar to Ref. 74 but for a different front lens. X-ray beamlines are or will be available at several existing or forthcoming FELs (FLASH and the European XFEL in Hamburg/Germany, SACLA in Japan, LCLS-II in Stanford/USA, and FREIA in Uppsala/Sweden). In particular, the development aims at five-dimensional k-space tomography  $I(\mathbf{k}, E_B, \Delta t)$ , with  $\Delta t$  denoting the intrinsic time scale of the ultrafast process under study. Tunable soft (or hard) x rays are necessary for addressing the  $k_z$ -component via proper setting of the photon energy.<sup>75</sup>

#### D. Space-charge suppression for different photoelectron kinetic energies

Trajectory patterns like in Fig. 3 obey the following symmetry law: If all voltages and the initial kinetic energy are multiplied



by the same factor, the patterns look identical. This means that the same approach can be used at lower energies, which is relevant for the rapidly growing branch of laboratory-based experiments with HHG sources. In practice, however, the desired effect is weaker at low  $E_{\text{kin}}$  because all other factors also scale: The natural separation of fast and slow electrons in the initial phase close to the sample surface takes longer. The retarding field is weaker; hence, the *slow-e-fast-e* Coulomb interaction persists longer. The saddle point is less pronounced, resulting in a weaker high-pass-filter effect. The observable  $k_{\parallel}$ -range is smaller because the geometry of the front lens limits the entrance angle. The chromatic aberration is larger; hence, the well-focused energy interval is narrower.

In order to elucidate the usefulness of the *repeller-MM* at lower energies, we made a survey study for three kinetic energies using the multimode lens described in Sec. III C (optimized for high energies). The trend is quantified in Figs. 4(a)–4(e), showing the results of time-resolved trajectory simulations for photoelectrons with  $E_{\text{kin}} = 1.5$  keV, 150 eV, and 25 eV plus slow electrons of 3 and 1 eV (blue and green trajectories, respectively). For simulation of the different kinetic energies, we made use of the scaling behavior, i.e., the trajectories for  $E_{\text{kin}} = 1.5$  keV, 150 eV, and 25 eV look identical [Fig. 4(a)]. However, the energy of the slow electrons does *not* scale, and in turn, their trajectories for the three cases look dramatically different in Figs. 4(c)–4(e). Obeying energy conservation, the slow electrons reach the zenith of their path at  $z_{\text{max}} = E_{\text{kin}}/eF$ . At high energies, the suppression is very effective, e.g.,  $z_{\text{max}} = 5$   $\mu\text{m}$  for photoelectrons with  $E_{\text{kin}} = 3$  keV and mPPE electrons of 3 eV and an optimized field of  $F = -600$  V/mm.

For  $E_{\text{kin}} = 1.5$  keV in Figs. 4(a)–4(c), the retarding field at the chosen setting is  $F = -230$  V/mm. The 3 eV electrons reach  $z_{\text{max}} = 13$   $\mu\text{m}$  after 25 ps; by then, the photoelectrons have traveled a distance of 0.5 mm. Within the first 5 ps, these photoelectrons have already reached a distance of 110  $\mu\text{m}$ ; correspondingly, the time integral of the Coulomb force exerted by the slow electrons is relatively small. Note that according to Sec. III A, the force integral depends on the size of the pump spot. In a hypothetical hot spot at 50  $\mu\text{m}$  from the center of the ROI, a ray bundle of 5 eV is launched, reaching  $z_{\text{max}} = 22$   $\mu\text{m}$  at 33 ps. The slow electrons from the hot spot only act on those photoelectrons, which started in the immediate vicinity of the hot spot (red ray bundles). The photoelectrons emitted in the ROI [40  $\mu\text{m}$  diameter, marked on the left side of Fig. 4(c)] do not feel significant forces from the slow-electron cloud at the hot spot. There is no “crosstalk” of photoelectrons emitted inside the ROI with slow electrons emitted in some distance, here 50  $\mu\text{m}$ , such as present in the case of the *long-range space-charge effects* of the *extractor-MM* discussed above.

For  $E_{\text{kin}} = 150$  eV [Fig. 4(d)], the photoelectron velocity is a factor of 3.2 smaller and the retarding field is a factor of 10 weaker ( $-23$  V/mm). In turn, the zenith of the 3 eV electrons is ten times farther away from the surface ( $z_{\text{max}} = 130$   $\mu\text{m}$  reached after 200 ps). The photoelectrons in the central ROI will feel the slow electrons from the hot spot (red rays) still quite weakly, depending on the density of the charge cloud at the hot spot. Finally, at  $E_{\text{kin}} = 25$  eV [Fig. 4(e)], the electrons are another factor of 2.5 slower and the field is only  $F \approx -4$  V/mm. The 3 eV electrons thus reach  $z_{\text{max}} = 750$   $\mu\text{m}$ . The velocity of the photoelectrons is only a factor of 2.9 larger than that of the 3 eV electrons; hence, these electrons travel close to each other

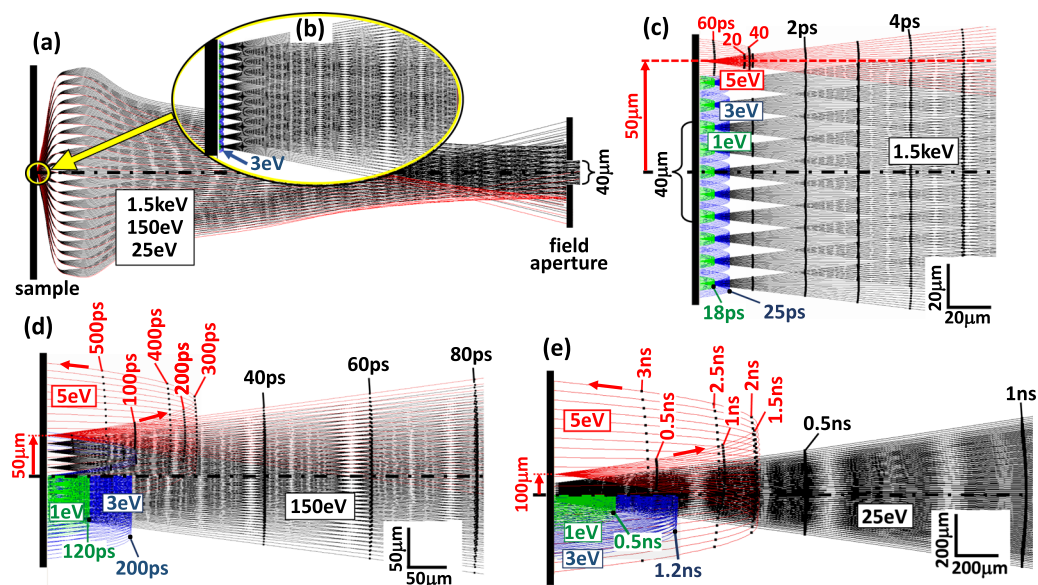


**FIG. 4.** Separation of fast and slow electrons in the repeller-lens mode for  $E_{\text{kin}} = 1.5$  keV, 150 eV, and 25 eV; the trajectories (a) look identical due to proportional lens settings. (b) shows the detail close to the sample surface with trajectories for the photoelectrons (black) and slow electrons (3 eV in blue, 1 eV in green). (c)–(e) Detail close to the sample for  $E_{\text{kin}} = 1.5$  keV, 150 eV, and 25 eV, respectively; here, a (point-like) hot spot is placed at 50  $\mu\text{m}$  [(c) and (d)] or 100  $\mu\text{m}$  (e) off-center (emitting 5 eV electrons, red trajectories). The repelling effect drops dramatically with decreasing  $E_{\text{kin}}$ , as visible in the increase in  $z_{\text{max}}$  from 13 to 750  $\mu\text{m}$  and interaction time from tens of ps to  $>1$  ns. The Moiré patterns are an artifact of the simulation.

for a long distance. During the correspondingly long interaction time, the photoelectrons emitted in the ROI might feel the Coulomb force by slow electrons from the hot spot, here located at  $100\ \mu\text{m}$  from the center of the ROI [Fig. 4(e)]. There is no free choice of the retarding field, since the parameter space for the focusing condition restricts the possible ratio between  $E_{\text{kin}}$  and the potential of the first lens element (variability  $\sim 30\%$ , higher field at the expense of the observable k-range). However, additional steering electrode(s) like in Fig. 3(b) allow generating a strong retarding field just in the region very close to the sample surface, which converts into an accelerating field at typically  $z \approx 1\ \text{mm}$ .

The results of many systematic simulations like those shown in Fig. 4 have finally led to the design of the new electron optics of the *repeller-MM*. The figure captures the essence of the action of the retarding field on the different electron “species.” In particular, it makes clear that space-charge suppression works best at high kinetic energies because then the reduction of the slow electrons’ velocity happens much more rapidly [compare the time scales in Figs. 4(c) and 4(e)].

In the *extractor-MM* mode, all slow electrons including those from hot spots are pulled into the lens system. In turn, hot spots contribute to the space-charge shift even if they are hundreds of  $\mu\text{m}$  away from the ROI, which is the signature of the long-range shift [Fig. 2(d)]. In the *repeller-MM*, this long-range effect is completely eliminated because the slow electrons are removed from the photoelectron beam close to the sample. The short-range shift explained in Fig. 2(a) is not completely suppressed but strongly reduced by the retarding field. Instead of long-living, expanding mPPE and SE charge clouds, we encounter short-living thin disks. In the case of  $1.5\ \text{keV}$ , these disks travel just  $13\ \mu\text{m}$  before they turn around, with lifetimes of  $\sim 50\ \text{ps}$  for  $3\ \text{eV}$  electrons and  $\sim 35\ \text{ps}$  for  $1\ \text{eV}$  electrons [Fig. 4(c)]. The retarding field rapidly reduces the average velocity of the disk, with the slower electrons reaching their zenith earlier than the fast ones (see simulations for  $1$ ,  $3$ , and  $5\ \text{eV}$  in Fig. 4). The asymmetric deceleration/acceleration effect vanishes already when the average velocity of the electrons within the disk becomes zero.

A key feature of the *repeller-MM* mode concerns the action of the *field aperture* (FA). The first lens group forms a magnified image of the sample surface in the FA plane. In Fig. 4, the magnification is 12 so that the assumed FA of diameter  $500\ \mu\text{m}$  selects a ROI of  $40\ \mu\text{m}$  on the sample [Figs. 4(a) and 4(b)]. The “crosstalk” of space-charge influence by slow electrons starting in some distance of the ROI [like the hot spot in (c)] is strongly reduced due to the repelling of the slow electrons. Hence, only slow electrons emitted inside the ROI contribute to the space-charge shift, unlike the situation in field-free photoemission and *extractor-MM*, where all slow electrons contribute.

The lens geometry studied in Figs. 3 and 4 is designed for kinetic energies in the soft x-ray range. Optimization for low energies needs more complex field distributions with more electrodes, which could improve the situation of Fig. 4(e) quantitatively. However, the trend of a strong worsening of the suppression effect with dropping energy is inherent to the method. As an example, Fig. 3(b) shows a four-electrode geometry, i.e., sample, repeller (1), accelerator (2), and steering electrode (3), providing more flexibility. BFP is the backfocal plane, hosting the first k-image. The simple sample-extractor-focus design of a conventional PEEM can be operated in

the retarding mode, but the k-field observable with this “reversed” PEEM lens is strongly restricted.

## IV. EXPERIMENTAL RESULTS

### A. Space-charge suppression in a pump-probe experiment in the XUV range

A first pilot study of the space-charge suppression mode has been performed using the IR pump-FEL probe setup of the HEXTOF microscope<sup>17</sup> at beamline PG2<sup>78,79</sup> of the free-electron laser FLASH (at DESY Hamburg). This instrument comprises the standard (low-energy) lens system without the steering electrode. The measurements were carried out at room temperature with a W(110) sample using IR pump pulses of  $1030\ \text{nm}$  [ $h\nu_{\text{pump}} = 1.20\ \text{eV}$ ; p-polarized] at pump fluences up to  $42\ \text{mJ}/\text{cm}^2$  ( $80\ \text{fs}$  pulse width) and XUV probe pulses of  $h\nu_{\text{probe}} = 111.6\ \text{eV}$  ( $\sim 100\ \text{fs}$  width). The results are shown in Figs. 5–7.

Figure 5 shows a result for the *long-range space-charge effect* in a pump-probe delay range  $\Delta t = -2$ – $26\ \text{ps}$ . The photoelectron intensity, integrated over the full k-field-of-view, is displayed as  $E_{\text{final}}$ -vs- $\Delta t$  plot for the *repeller-MM* mode with the front electrode at  $-85\ \text{V}$  [Figs. 5(a)–5(d)] and *extractor-MM* mode with the front electrode at  $+8\ \text{kV}$  [Figs. 5(e)–5(h)]. The final-state energy  $E_{\text{final}}$  is referenced to the position of the Fermi-energy cutoff (dashed horizontal line) in the undistorted case [Figs. 5(a)–5(c)], corresponding to a kinetic energy of  $E_{\text{kin}} = 107\ \text{eV}$ . In order to emphasize the energy shift and broadening, the same data arrays are shown on a logarithmic intensity scale for the region above  $E_F$  [Figs. 5(a) and 5(e)] and around the lower edge of the d-band [Figs. 5(b) and 5(f)]. Figures 5(c) and 5(g) show the full d-band region on a linear intensity scale, and the details [Figs. 5(d) and 5(h)] are shown with enhanced contrast. Note the factor of 2 between the  $E_{\text{final}}$ -scales in panels (a), (b), (e), and (f) and panels (c), (d), (g), and (h). The logarithmic plots offer a large enhancement of the dynamic range, as discussed in Ref. 46. This emphasizes the weak spectral features above and below the valence band.

The results in the first column of Fig. 5 have been recorded with the front electrode at  $-85\ \text{V}$  (corresponding to a field of  $F = -21\ \text{V}/\text{mm}$ ) and a pump-laser fluence of  $13\ \text{mJ}/\text{cm}^2$ . The  $E_{\text{final}}$ -vs- $\Delta t$  pattern [(a) and (c)] shows a sharp Fermi edge, and the only feature is the side bands due to laser-assisted photoemission (LAPE).<sup>80,81</sup> These side bands behave like photoemission with effective photon energies of  $h\nu_{\text{probe}} \pm n h\nu_{\text{pump}}$  ( $n$ : integer). The LAPE sidebands are visible as a narrow peak at  $\Delta t = 0$  and provide a marker for delay-time zero. Intensity spectra at  $\Delta t = -300\ \text{fs}$  (i),  $\Delta t = 0$  (j), and  $\Delta t = +300\ \text{fs}$  (k) reveal that the LAPE-signals above  $E_F$  appear only at  $\Delta t = 0$ , enlarged in the inset of (j). Strong contrast enhancement reveals that there is a weak signal of excited electrons on the right side ( $\Delta t > 0$ ) of the LAPE peak (d). The spectrum at larger time delay,  $\Delta t = 3\ \text{ps}$  (l), reveals a width of the Fermi edge of  $153\ \text{meV}$  (FWHM of the derivative). The FEL pulse energy was quite high for these measurements, giving rise to a residual space-charge effect in terms of bulging of the Fermi cutoff  $< 100\ \text{meV}$ , visible in the k-resolved patterns. After correction of this deformation, the fit of the Fermi edge shows a total width of  $120\ \text{meV}$ . Deconvolution with thermal broadening at room temperature ( $100\ \text{meV}$ ) and bandwidth of the FEL beam ( $58\ \text{meV}$ ) yields a value of  $\sim 30\ \text{meV}$  resolution for the ToF detector of the microscope.

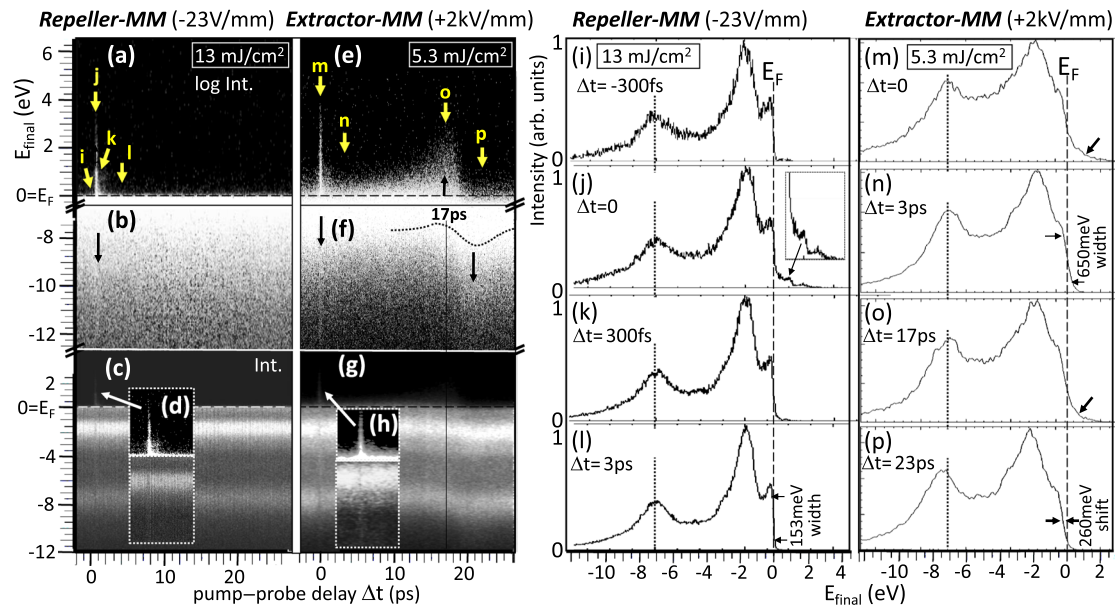


**FIG. 5.** Suppression of the *long-range space-charge artifact* in the retarding lens mode (*repeller-MM*) with field  $F = -21$  V/mm [(a)–(d)] in comparison with the conventional mode (*extractor-MM*) with the accelerating field  $+2$  kV/mm [(e) and (h)]. Data taken for a W(110) sample at room temperature, photon energies  $h\nu_{\text{pump}} = 1.2$  eV (p-polarized) and  $h\nu_{\text{probe}} = 111.6$  eV, recorded with the HEXTOF at the free-electron laser FLASH (DESY, Hamburg). The k-integrated photoelectron intensity distributions  $E_{\text{final}}$ -vs- $\Delta t$  are displayed on a logarithmic [(a), (b), (e), and (f)] and linear intensity scale [(c), (d), (g), and (h)]. The log scale emphasizes the region above  $E_F$ .  $E_{\text{final}} = 0$  ( $=E_F$ ) corresponding to  $E_{\text{kin}} = 107$  eV is calibrated at the Fermi edge of the “space-charge-suppressed” case (c). (i)–(p) Intensity spectra taken at the positions marked in (a) and (e).

Figures 5(e)–5(h) show the analogous results for the *extractor-MM* mode with an extractor voltage 8 kV (field  $F = +2$  kV/mm) and pump-laser fluence  $5.3$  mJ/cm<sup>2</sup>. The difference between the first and second column of Fig. 5 appears eye-catching in the logarithmic plots (a), (b), (e), and (f). The long-range space-charge interaction blurs the energy distribution and causes an energy shift. In particular, it imprints a characteristic artifact structure with maximum at  $\sim 17$  ps [black arrow in (e)] and an s-shaped profile with the inflection point at  $19.5$  ps and minimum around  $21$  ps [dotted curve and right arrow in (f)]. Note that the s-shaped artifact shifts the entire  $d$ -band and is well visible at its lower edge at  $E_{\text{final}} \approx -10$  eV [see (g)]. In addition, the LAPE peak (at  $\Delta t = 0$ ) appears at the lower edge due to the minus sign in the effective photon energy [left arrow in (f)]. The pronounced space-charge artifact with maximum at  $17$  ps and a change from accelerating to retarding net force around  $20$  ps was predicted by the simulation in Fig. 2(d) using identical input parameters.

The spectra [Figs. 5(m)–5(p)], taken in the *extractor-MM* mode, are significantly broadened; details such as the sharp peak right below  $E_F$  are washed out because the width of the Fermi edge increased to  $650$  meV [compare (l) and (n)]. In turn, the “discrete” characteristic of the LAPE signal is smeared out [compare (j) and (m)]. The s-shaped artifact causes an enhancement of the intensity above the Fermi edge [arrow in (o)] and a shift by  $260$  meV to lower kinetic energies in (p). The measurement in the retarding mode [(a)–(d)] was recorded at a higher pump fluence ( $13$  mJ/cm<sup>2</sup>) in comparison to the accelerating mode [(e)–(h)] ( $5.3$  mJ/cm<sup>2</sup>). Note that the SE always trail behind and thus can only exert accelerating

forces on the photoelectrons, which do not depend on pump–probe delay; this case is treated in detail in Ref. 48.

The s-shaped profile constitutes a “delay-time clock.” In practical work, the artifact maximum can indeed be exploited as a coarse measure for the position of true delay time zero.<sup>17</sup> For a given lens geometry, the coincidence position depends on the potential of the anode (extractor) and the photoelectron kinetic energy. From simulations, we estimate that when the extractor voltage is doubled from  $8$  to  $16$  kV (at  $E_{\text{kin}} = 107$  eV),  $\Delta t$  decreases from  $17$  to  $10$  ps; when  $E_{\text{kin}}$  is doubled from  $107$  to  $214$  eV (at an extractor voltage of  $8$  kV),  $\Delta t$  increases to  $\sim 25$  ps. For comparison, at  $E_{\text{kin}} = 25$  eV (typical for HHG experiments),  $\Delta t$  shrinks to  $\sim 7$  ps, corresponding to a distance of only  $200$   $\mu\text{m}$  between the slow and fast wavefronts, if the electrons are released at the same instant.

The *short-range space-charge effect* has been studied in a similar way in a region of  $\sim 4$  ps width around delay-time zero; the results are summarized in Fig. 6. Here, the pump fluence was set to  $0$ ,  $13$ ,  $22$ ,  $35$ , and  $42$  mJ/cm<sup>2</sup> for panels (a), (b), (c), (d), and (e), respectively. In order to ensure comparable conditions, the delay stage was also scanned for zero fluence. The sequence of k-integrated photoelectron intensity distributions shows  $E_{\text{final}}$ -vs- $\Delta t$  on a logarithmic (top row) and linear intensity scale (second row). As in Fig. 5, the logarithmic scale emphasizes differences in the weak-intensity region above  $E_F$ . Note the factor of 2 in the energy scales.

For pump fluences up to  $13$  mJ/cm<sup>2</sup> [Figs. 6(a) and 6(b)], there are no significant indications of space-charge effects. The corresponding spectra [(i)–(k)] for  $13$  mJ/cm<sup>2</sup> and [(f)–(h)] for  $5$  mJ/cm<sup>2</sup> (not shown in the upper part) reveal a sharp Fermi edge at  $\Delta t < 0$



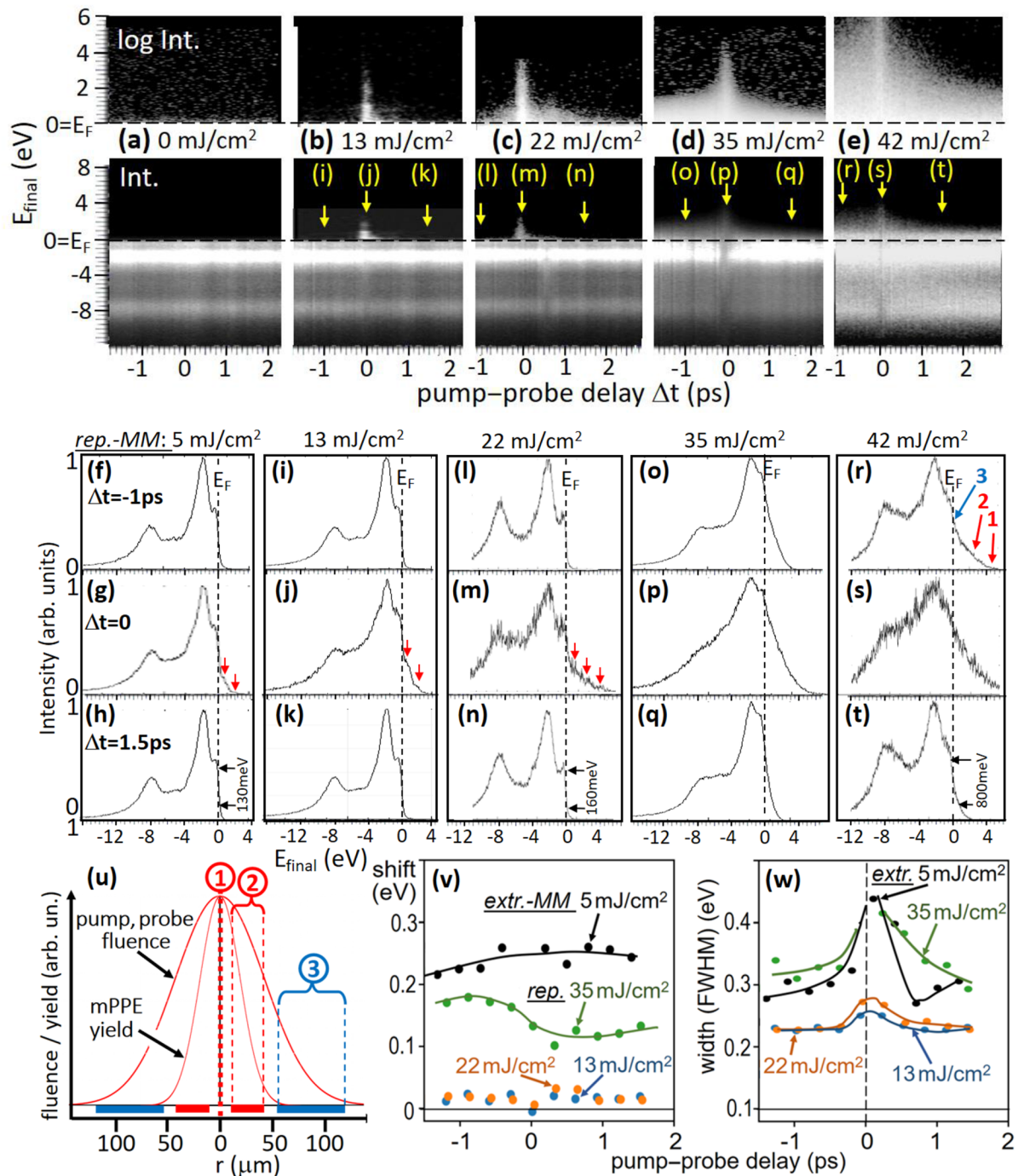


**FIG. 6.** Short-range space-charge effects recorded in the repeller-MM mode (*repeller-MM*) with field  $F = -21$  V/mm. Data taken for a W(110) sample at photon energies of  $h\nu_{\text{pump}} = 1.2$  eV (p-polarized) and  $h\nu_{\text{probe}} = 111.6$  eV using the HEXTOF at FLASH. The k-integrated photoelectron intensity distributions  $E_{\text{final}}$ -vs- $\Delta t$  [(a)–(e)] are displayed on a logarithmic (top row) and linear scale (second row); pump fluences stated in the panels.  $E_{\text{final}} = 0$  corresponding to  $E_{\text{kin}} = 107$  eV is calibrated at the Fermi edge of the “unpumped” case (a). (f)–(t) Intensity spectra extracted as line scans at pump-probe delays  $\Delta t$  as marked by arrows in panels (b)–(e). The columns refer to different pump fluences as stated on top, rows for  $\Delta t = -1$  ps, 0, and +1.5 ps. (u) Radial profiles of pump and probe fluences as well as mPPE yield; profiles schematic but radial coordinate  $r$  approximately like in the experiment. The yield curve of the 5PPE signal has a width about 2.2 times narrower than the curve of the pump fluence profile. Regions 1, 2, and 3 correspond to maximum mPPE space charge, radially dropping space charge, and zero mPPE space charge, respectively. Corresponding regions in the spectrum are marked in (r). (v) and (w) Shift and width of the Fermi edge as a function of pump-probe delay for the *extractor-MM* mode at a fluence of 5 mJ/cm² (black dots) and the *repeller-MM* mode at fluences between 13 and 35 mJ/cm² (colored dots); curves are to guide the eye.

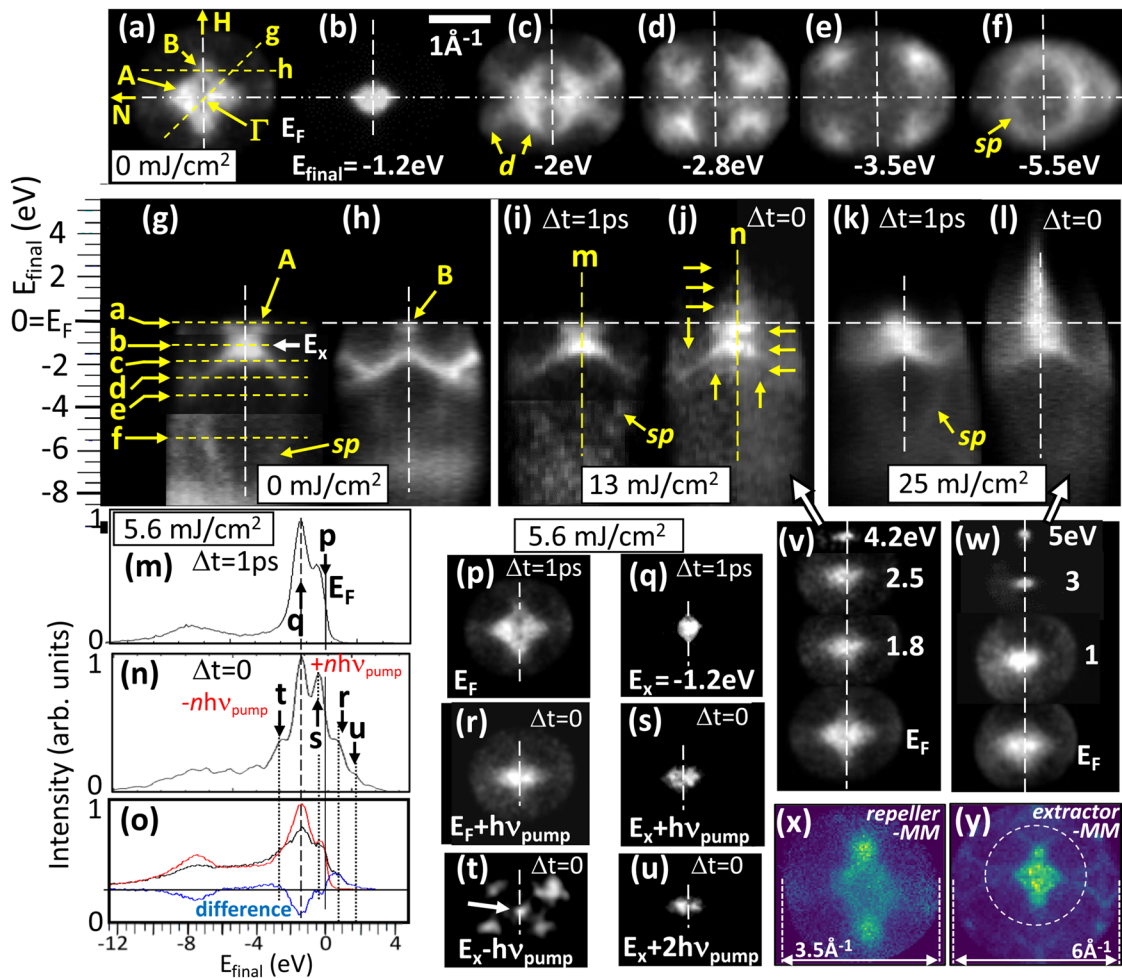


**FIG. 7.** Sections through the 4D ( $k_x$ ,  $k_y$ ,  $E_{\text{final}}$ ,  $\Delta t$ ) data arrays in the valence-band range of W(110) recorded at room temperature in the *repeller-MM* mode (field  $F = -21$  V/mm) with  $h\nu_{\text{pump}} = 1.2$  eV (p-polarized) and  $h\nu_{\text{probe}} = 111.6$  eV. (a)–(f)  $k_x$ – $k_y$  sections at different final-state energies as given in the panels and marked in (g); for the  $k$ -range, see scale bar, pump fluence 0. [(g) and (h)] Sections of final-state energy  $E_{\text{final}}$  vs.  $k_{\parallel}$  along the dashed lines in (a), showing the intense  $d$ -bands and the weakly visible  $sp$ -band. A and B in (a), (g), and (h) mark two prominent  $d$ -band features (see text). (i)–(l) Same for pump fluences of 13 mJ/cm<sup>2</sup> [(i) and (j)] and 25 mJ/cm<sup>2</sup> [(k) and (l)] at pump–probe delays of  $\Delta t = 1$  ps and 0. (m) and (n) Energy spectra along the vertical dashed lines in (i) and (j) but for pump fluence 5.6 mJ/cm<sup>2</sup>; (o) difference spectrum (blue), emphasizing excess and deficient intensity. (p) and (q)  $k$ -patterns at  $E_F$  and  $E_x$  [crossover point in (g)] for  $\Delta t = 1$  ps; (r)–(u) LAPE signatures at  $\Delta t = 0$  for the given energies. (v) and (w) Sequences of  $k_x$ – $k_y$  cuts through  $E_F$  and the LAPE signals in (j) and (l). (x) and (y) comparison of the  $k$ -field of view for the *repeller-MM* and *extractor-MM* mode for identical conditions.

(integrated between  $-0.6$  and  $-1$  ps) and  $\Delta t > 0$  (integrated between  $+1.3$  and  $+1.7$  ps). The LAPE signal shows up in terms of two shoulders above  $E_F$  [red arrows in (g) and (j)]. At 22 mJ/cm<sup>2</sup> (c), the pattern on the logarithmic scale (top row) shows additional weak intensity within  $\sim 1$  ps to both sides of the LAPE peak. The corresponding spectra [(l) and (n)] still show a sharp Fermi edge and a very small excess intensity at their high-energy tail. The spectrum at  $\Delta t = 0$  (m) extends to  $>4$  eV above  $E_F$  with the LAPE “steps” less resolved than at the lower fluences. At 35 and 42 mJ/cm<sup>2</sup> [(d) and (e)], the space-charge-induced changes are large and visible already on the linear intensity scale. The excess intensity drops within few ps on both sides of the LAPE peak and shows a clear trend in the

sequence [Figs. 6(c)–6(e)], which can be understood in the light of Figs. 2(a) and 4.

The spectra [Figs. 6(o)–6(t)] reveal interesting details, shining light on the nature of the residual space-charge effect in the *repeller-MM* mode. In the unpumped spectrum, the region near  $E_F$  shows a shoulder followed by the sudden drop of the Fermi cutoff [visible, e.g., in (n)]. At the high fluences, this signature of shoulder and steep drop is still visible at the same kinetic energy [e.g., in (t)]. In addition, a long wing toward high energies appears, reaching 2 eV in spectrum (t) (integrated between  $\Delta t = +1.3$  and  $1.7$  ps) and even to  $>4$  eV in spectrum (r) (integrated between  $\Delta t = -0.6$  and  $-1$  ps). On this short time scale, we do not observe a rigid shift of the



valence-band spectrum as in the *extractor-MM* measurement in Fig. 5(g), where the entire *d*-band shows the s-shaped shift. The long-range effect is completely eliminated because no slow electrons can cross the first electrode.

The  $E_{\text{final}}$ -vs- $\Delta t$  plots in the sequence [Figs. 6(c)–6(e)] show the trend in the temporal behavior. With increasing fluence, the energy gain increases, reflecting the increasing strength of the Coulomb forces with increasing mPPE charge. The energy gain is strongest at  $\Delta t = 0$  (on both sides of the LAPE peak) and it is higher for negative delay. All these signatures agree with the prediction of the model in Sec. III A. However, the energy shift drops much faster than expected from the model in Fig. 2(a) and from Eq. (1). The half width of  $\sim 1.5$  ps in (e) is more than 2 orders of magnitude shorter than in the case of field-free photoemission.<sup>12,36,37</sup> This is the fingerprint of the *repeller-MM* mode and reflects that the velocity of the mPPE electrons is reduced on the micrometer scale. This happens very rapidly for very slow electrons with  $E_{\text{kin}} < 1$  eV, leading to a reduction of ratio  $\beta$  in Eq. (1).

The—at first sight puzzling—superposition of an unshifted and a strongly shifted and broadened spectrum [Fig. 6(r)] can be explained by considering the beam profiles. Figure 6(u) shows schematic radial profiles of fluences and mPPE yield. In this scheme, the pump and probe profiles are assumed to have the same FWHM (100  $\mu\text{m}$ ). The corresponding yield curve for the 5PPE transition then has a FWHM of only 45  $\mu\text{m}$ . This leads to a strongly inhomogeneous action of the mPPE-induced space charge. With increasing radius  $r$ , the yield drops rapidly from its maximum at (1) through a region of extremely strong radial variation of yield and hence varying space-charge action (2). Above  $r = 50$   $\mu\text{m}$  (3), the mPPE yield is practically zero, but the probe fluence is still significant. In turn, a ring-shaped region of “space-charge free” photoelectron emission exists (marked in blue). This weakly pumped region is the origin of the unshifted part of the spectrum for 42  $\text{mJ}/\text{cm}^2$  [(r) and (t)]. For this measurement, the field aperture was 2 mm, selecting a ROI of  $\sim 200$   $\mu\text{m}$  on the sample surface, and the probe beam was larger than the ROI, further enhancing the ratio of weakly pumped sample area.

The coexistence of the non-shifted Fermi edge and the broad high-energy wing up to  $E_{\text{final}} \approx 4$  eV in Fig. 6(r) provides important information: In the *repeller-MM* mode, there is indeed negligible “crosstalk” of the space charge from regions 1 and 2 into region (3), as we concluded from Fig. 4. In order to further validate this result, the data for 35  $\text{mJ}/\text{cm}^2$  [Figs. 6(o), 6(p), and 6(q)] have been recorded with a smaller field aperture of 1 mm, cutting away most of the unpumped region of  $r > 50$   $\mu\text{m}$ . In turn, the visible “kink” between the steep unshifted Fermi edge and broad wing in (r) has disappeared and the Fermi cutoff shows a continuous drop in spectra [(o) and (q)]. As predicted by Figs. 2(a) and 2(b), the shift is largest for negative delay (first row of spectra) and smaller for positive delay (third row). For  $\Delta t = 0$ , the broadening is superimposed by the LAPE peaks (second row). In the *repeller-MM* mode at  $E_{\text{kin}} = 107$  eV, the desired ROI can be selected by the field aperture.

The data arrays of Fig. 6 can be quantitatively compared with a measurement in the *extractor-MM* mode. The results of this comparison are summarized in Figs. 6(v) and 6(w) in terms of the energy shift (v) and width (w) of the Fermi edge. Data are plotted as a function of pump-probe delay. The black dots show the results for the *extractor-MM* at 5  $\text{mJ}/\text{cm}^2$ , leading to an energy shift of

220–250 meV and width of 280–320 meV. For these measurements, the energy resolution was set to 220 meV. We do not discuss the LAPE peak here since it does not originate from the space-charge effect.

The corresponding results recorded in the *repeller-MM* mode are shown as colored dots. At 13 and 22  $\text{mJ}/\text{cm}^2$ , the shift is insignificant ( $\sim 20$  meV) and the width of the Fermi edge is not increased (except for the region of the LAPE peak). At 35  $\text{mJ}/\text{cm}^2$ , the shift exhibits an s-shaped profile with extrema of 180 and 120 meV at negative and positive time delays, respectively. The width has increased by  $\sim 100$  meV, slightly more than the value for the *extractor* mode. These shifts and broadenings are the residue of the short-range effect, which remains despite the repeller field, as explained in Fig. 4. The shift decreases toward positive delays, in accordance with the predictions of Sec. III A. The broad wing of the LAPE peak toward positive delays ( $> 1$  ps) in the 35  $\text{mJ}/\text{cm}^2$  measurement in Fig. 6(w) may contain a contribution of hot-electron lifetime, which we will not discuss here. When comparing the *repeller* mode at 35  $\text{mJ}/\text{cm}^2$  with the *extractor* mode at 5  $\text{mJ}/\text{cm}^2$ , we have to bear in mind that the corresponding 5PPE yield (which causes the shift and broadening) has increased by four orders of magnitude.

The large energy gain appears almost threshold-like between 22 and 35  $\text{mJ}/\text{cm}^2$  [compare Figs. 6(c) and 6(d)]. This reflects that the pump-induced electrons result from a highly non-linear mPPE transition. Quantitative evaluation revealed that shifts and broadening scale approximately with the third power of the pump fluence, and not with the fifth order as expected from the energy balance. We attribute this deviation to a Coulomb barrier caused by the high charge density in the mPPE disk, which repels electrons at the trailing edge of the disk and blocks further low-energy electrons to leave the sample. This barrier effect might reduce the gain in the tolerable slow-electron yield of the *repeller-MM* compared to the *extractor-MM* to three orders of magnitude. Even fractional exponents have been observed,<sup>52</sup> which moreover depend on the orientation of the electric vector of the pump beam. Likewise, electrons at the leading edge are accelerated, which leads to an increase in the ratio  $\beta$  in Eq. (1).

## B. Momentum-resolved study of the space-charge suppression mode

The measurements shown in Sec. IV A have been recorded in the *k*-resolving mode. Here, we refine the analysis by looking at the *k*-distributions. Figure 7 shows sections through the 4D ( $k_x$ ,  $k_y$ ,  $E_{\text{final}}$ ,  $\Delta t$ ) data arrays in the valence-band range of  $W(110)$ , all taken in the *repeller-MM* mode at  $h\nu_{\text{probe}} = 111.6$  eV. Each of the arrays was recorded in just 15 min. Since we discuss space-charge shifts and LAPE band replicas, the use of the energy scale  $E_{\text{final}}$  (with zero at the Fermi level in the unpumped case) is more appropriate than  $E_B$ . The top row shows a sequence of  $k_x$ – $k_y$  sections at different binding energies: Fig. 7(a) at  $E_F$ ; (b) at  $E_{\text{final}} = -1.2$  eV =  $E_X$ , the intense *d*-band crossover; (c) at  $-2.0$  eV, where the local bandgap at the  $\Gamma$ -point opens; (d) at  $-2.8$  eV, where four elliptical band features appear; (e) at  $-3.5$  eV, where the ellipses have contracted to four points; and finally (f) at  $E_{\text{final}} = -5.5$  eV, showing the parabolic *s*-band below the *d*-band complex. For this sequence, the pump beam was off. The second row shows  $E_{\text{final}}$ -vs- $k_{\parallel}$  sections through the same “unpumped” data array [(g) and (h)] and for pump fluences of

13 mJ/cm<sup>2</sup> [(i) and (j)] and 25 mJ/cm<sup>2</sup> [(k) and (l)]. The positions of sections [(g) and (h)] are indicated as dashed lines in (a).

Adopting the parameters from Ref. 75 (inner potential  $V_0^* = 10$  eV, referenced to  $E_F$ ; effective mass  $m_{\text{eff}} = 1.07m_e$ ), we derive the final-state momentum according to

$$k_{\text{final}} = \left(\frac{1}{\hbar}\right) \sqrt{2m_{\text{eff}} E_{\text{final}}}, \text{ with } E_{\text{final}} = \hbar\nu - E_B + V_0^*. \quad (3)$$

The resulting  $k_{\text{final}} \approx 5.93 \text{ \AA}^{-1}$  corresponds to  $2.1G_{110}$  ( $G_{110} = 2.81 \text{ \AA}^{-1}$  reciprocal lattice vector). Hence, the final-state energy isosphere intersects the bulk Brillouin zone very close to the  $\Gamma$ -H-N plane. The bright feature in the center of Fig. 7(a) is a cut through the octahedral electron pocket of the Fermi surface (A) and through the two electron balls (B) adjacent to the octahedron along the  $\Gamma$ -H direction. Both features contract with increasing binding energy (b), and the crossover of band A is characterized by a high intensity at  $E_B = 1.2 \text{ eV} = E_X$ ; the band dispersion is visible in section (g). Next to the intense  $d$ -bands, the parabolic  $sp$ -band is visible at enhanced contrast [(f) and lower part of (g)]. In agreement with the profiles through the Fermi edge [Fig. 6(n)], there is only a small smearing out of the band energies up to a fluence of 13 mJ/cm<sup>2</sup> [Figs. 7(i) and 7(j)]. The  $E_B$ -vs- $k_x$  section at 1 ps pump-probe delay (i) shows no significant influence of space charge, and only at 25 mJ/cm<sup>2</sup> (k), the space-charge shift and broadening are significant.

The pronounced valence-band dispersion and intense crossover point at  $E_X = 1.2 \text{ eV}$  are well suited for a  $k$ -resolved study of the LAPE effect; all measurements were done with the  $p$ -polarized pump beam. The  $E_{\text{final}}$ -vs- $k_x$  sections [Figs. 7(j) and 7(l)] show characteristic LAPE patterns at 13 and 25 mJ/cm<sup>2</sup>, respectively. At 13 mJ/cm<sup>2</sup>, the discrete nature of the LAPE transitions is clearly visible [horizontal arrows in (j)], whereas at 25 mJ/cm<sup>2</sup>, the discrete LAPE transitions are masked by space-charge broadening [Fig. 7(l)]. At the lower fluence of 5.6 mJ/cm<sup>2</sup>, the LAPE signature is better pronounced; hence, we analyzed this data array in detail [see results in Figs. 7(m)–7(u)]. The  $\Delta t = 1$  ps spectrum (m) through the  $\Gamma$ -point [like the vertical dashed line in (i), but for 5.6 mJ/cm<sup>2</sup>] is dominated by the high-intensity peak at the band crossover at  $E_X$ , adjacent to a shoulder toward the Fermi cutoff.

Important information concerning LAPE replicas results from low-energy measurements. For defect-free surfaces, the pump-induced electron signal originates from coherent mPPE and shows a series of “replicas” of the valence bands (see, e.g., Fig. 5 in Ref. 83). This replica effect breaks the paradigm that at low photon energies, the photoemission horizon is strongly restricted because mPPE (with sufficiently large  $m$ ) gives access to large in-plane momenta, involving optical transitions from the occupied to unoccupied bands (see Fig. 2 in Ref. 84). In turn, the energy and angular pattern of the mPPE electrons can be strongly structured, depending on the band structure.

The  $k_x$ - $k_y$  momentum pattern at the inflection point of the  $E_F$ -cutoff [Fig. 7(p)] shows the diamond-shaped bright central structure with two characteristic dark points above and below the center (along  $\Gamma$ -H). The pattern at the crossover energy  $E_X$  shows a very bright, small spot (q); for sake of counting statistics, (p) and (q) have been integrated over the pump-probe delay range  $>1$  ps. Spectrum (n), corresponding to  $\Delta t = 0$ , shows a number of shoulders to both sides of the crossover peak. The  $k_x$ - $k_y$  LAPE signatures

with one additional pump photon are found at energies  $E_F + \hbar\nu_{\text{pump}}$  (r) and  $E_X + \hbar\nu_{\text{pump}}$  (s). Pattern (r) shows the contour of the central diamond feature with enhanced intensity along the horizontal axis and (s) shows an intense feature close to the  $\Gamma$ -point. Toward lower binding energies, we find the bright crossover spot at energy  $E_X - \hbar\nu_{\text{pump}}$  [arrow in (t)] surrounded by the four bright spots visible in the unpumped pattern (e). Finally, at  $E_X + 2\hbar\nu_{\text{pump}}$  (u), the bright central crossover peak appears again. As expected, the LAPE process leads to replica-like repetition of the band features; the vertical arrows in Fig. 7(j) indicate faint traces of replicas of the downward-dispersing band to both sides. The weakness of these structures and the apparent double spots in (s) and (t) can be attributed to the limited counting statistics. The sequences taken at higher fluences of 13 mJ/cm<sup>2</sup> (v) and 25 mJ/cm<sup>2</sup> (w) show a gradual merging of the diamond pattern at  $E_F$  and the bright spot at  $E_X$ . The high final-state energy of  $>4 \text{ eV}$  above  $E_F$  in (l) suggests that four pump photons are involved in the highest LAPE signal.

The  $d$ -band features can be compared with previous experiments in the low-energy<sup>82</sup> and soft x-ray range.<sup>75</sup> Note that for the geometry of the HEXTOF (“inverted PEEM lens” without steering electrode), the usable  $k$ -field in the retarding mode is restricted. In the present measurements at  $E_{\text{kin}} = 107 \text{ eV}$ , we observe a diameter of  $\sim 3.5 \text{ \AA}^{-1}$ , whereas switching the front lens to the acceleration mode yields a diameter of  $6 \text{ \AA}^{-1}$ ; see Figs. 7(x) and 7(y), respectively.

### C. Space-charge suppression in a large $k$ -field in high-energy photoemission

Giving access to the true bulk electronic structure, buried layers with protective capping, and functional layers of devices *in operando*, fs photon pulses with energies in the several-keV range will strongly widen the scientific horizon. Dramatic progress in hard x-ray photoemission, in general,<sup>85,86</sup> and hard x-ray momentum microscopy, in particular,<sup>29–31,74,87,88</sup> has laid the cornerstone for fs time-resolved hard x-ray ARPES (tr-HARPES). It is clear that the pump-probe scheme will work at high energies. However, the question remains whether such large retardation factors are possible without strong image distortions. High retarding fields in the order of  $-1 \text{ kV/mm}$  will allow for even higher pump fluences, as those shown in Fig. 6. The feasibility of the space-charge suppression mode at higher energies has been studied using ps x-ray pulses from PETRA III (beamline P22,  $\hbar\nu = 3835 \text{ eV}$ ,  $p$ -polarized). This was no pump-probe experiment, but rather a proof-of-principle that the retarding mode works very well at high energies and correspondingly high retarding fields, here  $-600 \text{ V/mm}$ .

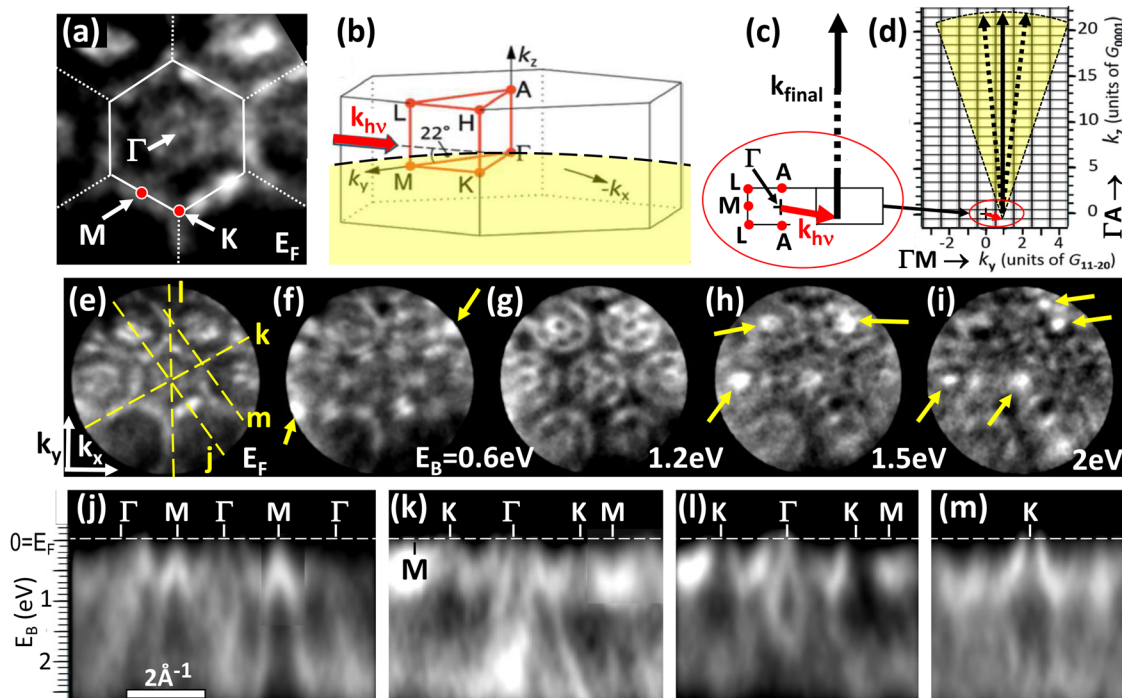
At such high energies, the advantages of the retarding mode are evident. First of all, the natural separation of the true photoelectrons from the slow electrons proceeds much faster [numbers are given in Sec. II A and Figs. 4(a)–4(c)]. The retarding field scales essentially linearly with the photoelectron kinetic energy. For  $E_{\text{kin}} = 3 \text{ eV}$  and retarding field  $F = -600 \text{ V/mm}$ , the slow electrons reach the zenith of their path [and hence  $v_0 = 0$  in Eq. (1)] already at  $z_{\text{max}} = 5 \text{ \mu m}$ . Thanks to the fast drop of the velocity of the slow-electron disk, the space-charge shift is very small. Despite the geometric constraints induced by the retarding front lens, the usable transversal momentum range  $k_{\parallel\text{max}} = 0.521 \sin \theta / \sqrt{E_{\text{kin}}}$  ( $\theta$ , emission angle from the sample) is quite large at high energies. Related to this, the depth of focus is much larger than at low energies.

Figure 8 shows a measurement at  $h\nu = 3835$  eV using the standard high-energy MM without steering electrode, demonstrating the retarding mode at high field strength and large  $k$ -field of view, here  $\sim 7 \text{ \AA}^{-1}$  diameter. The 3D ( $k_x$ ,  $k_y$ ,  $E_B$ ) data array has been recorded for a Re(0001) sample in the  $\Gamma$ -K-M plane; the Brillouin zone and high-symmetry points are marked in the  $k_x$ - $k_y$  section, Fig. 8(a). The photon energy was adjusted so that this section runs through the center of the BZ, as sketched by the dashed contour in Fig. 8(b). Bandmapping at such high energies is characterized by some peculiarities, which deserve short consideration. We describe the transition in a  $k$ -space picture that naturally includes the transfer of photon momentum  $k_{h\nu} = 2\pi\nu/c$  to the photoelectron<sup>89</sup> [see details in Fig. 8(c)]. Owing to energy conservation, all final states are located on a sphere with radius  $k_{\text{final}}$ ; this is the “free-electron-like” aspect. However, the final state is by no means a free-electron state because the transition happens in the bulk and the final state has to be described in the periodic zone scheme.

The sketch in Fig. 8(d) shows how the final-state sphere intersects the extended periodic scheme of the electronic bands. The dashed arrows mark the observable  $k$ -range, covering about 3 BZ-diameters. Assuming an inner potential of  $V_0^* = 10$  eV and  $m_{\text{eff}} = m_e$  (valid at such high energies),  $E_{\text{final}} = 3845$  eV (relevant is

the final-state energy inside of the material, including  $V_0^*$ ) corresponds to  $k_{\text{final}} = 31.73 \text{ \AA}^{-1}$  [cf. Eq. (3)]. The reciprocal lattice vector perpendicular to the surface is  $|\mathbf{G}_{0001}| = 1.410 \text{ \AA}^{-1}$ ; hence, the transition leads to the 22<sup>nd</sup> repeated BZ along the [0001]-direction. The photon momentum is  $k_{h\nu} = 1.95 \text{ \AA}^{-1}$ , which is of the order of the in-plane lattice vector  $|\mathbf{G}_{11-20}| = 2.276 \text{ \AA}^{-1}$ . The vector  $\mathbf{k}_{h\nu}$  [red arrow in Fig. 8(c)], tilted by  $22^\circ$  due to the photon impact] thus causes a strong displacement of the center of the final-state energy isosphere from the  $\Gamma$ -point  $\mathbf{k} = (0, 0, 0)$  far into the adjacent repeated BZ. The condition that energy conservation *and* momentum conservation have to be fulfilled independent of each other, in addition to the momentum-space periodicity (photoemission is an Umklapp process), leads to a complex behavior, which can best be visualized in a  $k$ -space model and best be observed looking directly into  $k$ -space. In addition, valence-band photoelectron diffraction being either intrinsic in the photo-transition (Laue-type) or extrinsic (Kikuchi-type)<sup>89</sup> adds another level of complexity.

Figure 8(d) shows the transition in the  $\Gamma$ -A-L-M plane of the repeated zone scheme; each of the small rectangles represents a BZ. Variation of  $k_z$  via the photon energy, alongside with ( $k_x$ ,  $k_y$ ) imaging and parallel ToF energy recording, allows a tomographic-like mapping of the bands in 4D ( $E_B$ ,  $\mathbf{k}$ ) parameter space.<sup>74,75</sup> When



**FIG. 8.** Sections through a 3D ( $k_x$ ,  $k_y$ ,  $E_B$ ) data array recorded for the valence-band of Re(0001) in the high-energy repeller-MM mode (field  $F = -600$  V/mm) at  $h\nu = 3835$  eV (without pump beam). The measurement was performed at beamline P22 of the synchrotron source PETRA III (DESY, Hamburg) using a high-energy time-of-flight momentum microscope. (a) Measured  $k_x$ - $k_y$  section at the Fermi energy with high-symmetry points and (b) perspective view of the hcp Brillouin zone of rhenium. [(c) and (d)] Photo-transition in  $k$ -space, with participation of the photon momentum  $\mathbf{k}_{h\nu}$  (oriented  $22^\circ$  off-plane) in the momentum balance.  $G_{0001} = 1.410 \text{ \AA}^{-1}$  and  $G_{11-20} = 2.276 \text{ \AA}^{-1}$  denote the two reciprocal lattice vectors in the drawing plane along  $\Gamma A$  and  $\Gamma M$ , respectively. (e)–(i)  $k_x$ - $k_y$  sections at different binding energies as stated in the panels;  $k$ -range diameter:  $7 \text{ \AA}^{-1}$ . Arrows mark local intensity enhancement by Laue-type photoelectron diffraction. (j)–(m) Corresponding  $E_B$ -vs- $k_{\parallel}$  sections revealing the band dispersions;  $k$ -scale denoted by high-symmetry points and scale bar in (j).



tuning  $k_{\text{final}}$  to the center of the 22nd BZ, the strong displacement of the sphere by the photon momentum must be accounted for. The dotted vectors in (d) mark the size of the  $k$ -field of view.

The sequence [Figs. 8(e)–8(i)] shows the momentum disks in the central and six adjacent BZs. Due to the curved final-state isoen-ergetic contour with the displaced center, the pattern is not precisely sixfold symmetric. The bottom row shows the band dispersions along four directions as marked in (e). The band patterns are dominated by the outward-dispersing bands with bright maxima at the M-points (j), a steep band maximum at  $\Gamma$ , surrounded by an inward-dispersing band (k), and local band gaps at the K-point [(l) and (m)]. A full analysis of the surface states and bulk bands of Re(0001) is given in Ref. 90.

The eye-catching bright regions marked by arrows in Figs. 8(f), 8(h), and 8(i) are fingerprints of Laue-type valence band photo-electron diffraction.<sup>89</sup> These local intensity enhancements form an irregular pattern of “reflexes” moving through 3D  $k$ -space, when the energy is varied [see the sequence (e)–(i) and bright regions in (k) and (l)]. For this measurement, we used the Si(111) monochroma-tor crystal of beamline P22, providing a moderate energy resolution of 350 meV,<sup>91</sup> which also downgrades the  $k$ -resolution. Using the (311) crystal, the resolution is a factor of 3 better.

## V. SUMMARY AND CONCLUSIONS

Space-charge effects in pump–probe photoemission have been always a limiting factor to be considered in designing and per-forming such experiments. Most importantly, pump-induced space charge has limited applicable excitation fluences compared to other experimental techniques, complicating comparative studies<sup>13,92</sup> or even preventing the investigation of certain materials or effects such as photoinduced phase transitions<sup>93</sup> or photoelectron diffrac-tion. Here, we present a novel approach for the suppression of space-charge effects, thereby allowing us to considerably increase usable pump (and probe) fluences in photoemission experiments. A retarding electric field at the sample surface repels the slow pump-induced electrons (in typical experiments  $10^4$ – $10^6$  e/pulse) back to the surface, substantially reducing the integral Coulomb force on the escaping photoelectron. The basic idea is confirmed by time-resolved ray-tracing simulations and analytical modeling, exploit-ing that electron lenses can be both retarding or accelerating. The design studies resulted in a new type of objective lens in a momen-tum microscope (MM), capable of creating fields of both polarities at the sample surface. The concept was validated in a fs pump–probe experiment at the free-electron laser FLASH (at DESY, Hamburg).

In order to distinguish the new approach from the conventional extractor-based front lens in PEEMs and MMs, we term the new mode *repeller-MM*, opposed to *extractor-MM*. In the latter case, all slow electrons are pulled into the microscope column, causing long-range Coulomb interactions over tens of mm. In the *repeller-MM*, the slow electrons turn around after short distances between few  $\mu\text{m}$  and some 100  $\mu\text{m}$ , depending on the photoelectron kinetic energy (which determines the retarding field). In the early phase (few ps) after the probe pulse, the disk of pump-induced electrons and the positive surface charge can be considered as an expanding parallel-plate capacitor, whose negative plate moves at a velocity of  $\sim 1 \mu\text{m}/\text{ps}$ . For a given charge density, the potential difference increases linearly

with distance. For realistic conditions of a disk size of 100  $\mu\text{m}$  (given by the pump spot) and a charge of 100 fC in the disk, the capaci-tance drops from 0.05 to 0.03 pF in the time interval between 1 and 2 ps after the pump pulse, leading to an increase of the disk potential from  $-2$  to  $-3.3$  V. The fast photoelectron thus feels a weaker retard-ing force when it travels inside the capacitor and a stronger acceler-ating force after having crossed the charge disk. The force integral can be solved analytically assuming a monoenergetic charge cloud by employing the mirror charge model. The energy gain [Eq. (1)] is proportional to the disk potential and depends just on two param-eters, the velocity ratio of slow and fast electrons and the geometrical ratio of the disk diameter and its distance from the surface at the time when the probe pulse arrives. The systematic study at FLASH ( $h\nu_{\text{pump}} = 1.2$  eV;  $h\nu_{\text{probe}} = 111.6$  eV) revealed that the *repeller* mode at a pump fluence of 35 mJ/cm<sup>2</sup> causes practically the same space-charge-induced energy shift and broadening as the *extractor* mode at 5 mJ/cm<sup>2</sup>. The quantity relevant for space-charge effects is not the pump fluence but the *slow-electron yield* (here 5PPE yield). At the given conditions, the *repeller* mode thus permits three to four orders of magnitude higher slow-electron yield.

The key factor for the efficiency of the *repeller-MM* mode is the fast reduction of the *velocity* of the slow electrons (and not their complete removal). The reason is that the deterministic energy shift by the space-charge interaction is a *kinematic* effect originating not from the existence of many slow electrons but from their average velocity. The asymmetry of the forces experienced by the photoelec-tron when crossing the capacitor vanishes for a static disk because electrostatic forces are conservative. Binary *e-e* scattering events smear out energies and randomize momentum distributions, which can be considered as stochastic heating. Individual *fast e-fast e* scatter-ing events are negligible at typical probe fluences, but *slow e-fast e* scattering events are significant. Since they strongly reduce the kinetic energy of the fast electron, the scattered photoelectron drops out of the observation window. In addition, the high-pass filtering effect of the *repeller-MM* reduces the width of the energy spectrum and counteracts detector saturation.

We conclude with a **SWOT (strengths, weaknesses, opportu-nities, threats) analysis** of the retarding and accelerating lens mode. The key strength of the *repeller-MM* is its capability to work at much higher pump fluences, far beyond the present limits for photoe-mission experiments. Furthermore, the field aperture reduces the space-charge effect by confining the region of interest (ROI) and suppresses the influence of hot spots in some distance from the ROI (for  $E_{\text{kin}} \geq 100$  eV). The main weaknesses are the limited depth of focus, demanding sequential data recording (stacks with widths of 1–2 eV), and the smaller  $k$ -field of view (less than a typical BZ diam-eter at low  $E_{\text{kin}}$ ). The opportunities lie in the access of a previously prohibited regime of pump fluences, paving the way toward stud-ies of lattice dynamics via tr-XPD<sup>16,29</sup> and phase transitions that demand deposition of large amounts of energy.

Key strengths of the *extractor-MM* are the large depth of focus (simultaneous recording of intervals up to  $\sim 10$  eV) and the large  $k$ -field-of-view (diameters up to 20  $\text{\AA}^{-1}$ ). Its weakness is the high sensitivity to space-charge effects acting in the short- and long-range regimes (s-shaped artifact in Fig. 5), since all slow electrons are pulled into the column. Opportunities are the simultaneous obser-vation of a huge phase-space interval (all emitted electrons in full half space and complete  $d$ -band complex for  $E_{\text{kin}} \leq 70$  eV) and the

absence of any restrictions in the usable energy range from down to few eV to keV.

In both cases, the threat is the sensitivity to non-planar surfaces (e.g., due to imperfect cleaving) causing distortions of the electric field. This problem can only be solved in a third mode with zero field at the sample surface, as described in Ref. 74. The next generation of ToF MMs will be equipped with a multi-mode lens, allowing exploiting the advantages of the accelerating and retarding mode as well as the zero-field mode. The latter is favorable for 3D structured samples such as cleaved microcrystals or for large off-normal emission angle ranges.

## ACKNOWLEDGMENTS

We would like to thank M. Aeschlimann and B. Stadtmüller (TU Kaiserslautern), M. Reutzel (Univ. Göttingen), and R. Ernstorfer (Fritz-Haber-Institut, Berlin) for stimulating discussions and a critical reading of the manuscript. For excellent technical support, we thank A. Oelsner and team (Surface Concept GmbH, Mainz) and the scientific and technical staff of DESY (Hamburg, Germany), a member of the Helmholtz Association HGF, operating FLASH and PETRA III in an excellent way. We would also like to thank H. Meyer and S. Gieschen (University of Hamburg) for support of the HEXTOF instrument. We further thank the referee for drawing our attention to the importance of a quantitative comparison of the shift and broadening of the Fermi level in the extractor and repeller mode.

Financial support of the Mainz group from Bundesministerium für Bildung und Forschung (BMBF, Project Nos. 05K19UM1 and 05K19UM2) and Deutsche Forschungsgemeinschaft (German Research Foundation), Grant No. TRR 173 “Spin+X” 268565370 (Project A02), is gratefully acknowledged. The work of the groups in Hamburg and Kiel was funded, in part, by the Deutsche Forschungsgemeinschaft within the framework of the Collaborative Research Center SFB 925-170620586 (Project No. B2). T.K.A. acknowledges support from the U.S. Department of Energy, Basic Energy Science, Contract No. DE-SC0016017. L.R. acknowledges funding by the Deutsche Forschungsgemeinschaft within the Emmy Noether Program (Grant No. RE 3977/1).

## DATA AVAILABILITY

The data that support the findings of this study are available from the corresponding author upon reasonable request.

## REFERENCES

- 1 T. Rohwer, S. Hellmann, M. Wiesenmayer, C. Sohr, A. Stange, B. Slomski, A. Carr, Y. Liu, L. M. Avila, M. Kalläne, S. Mathias, L. Kipp, K. Rossnagel, and M. Bauer, “Collapse of long-range charge order tracked by time-resolved photoemission at high momenta,” *Nature* **471**, 490 (2011).
- 2 F. Schmitt, P. S. Kirchmann, U. Bovensiepen, R. G. Moore, L. Rettig, M. Krenz, J.-H. Chu, N. Ru, L. Perfetti, D. H. Lu, M. Wolf, I. R. Fisher, and Z.-X. Shen, “Transient electronic structure and melting of a charge density wave in  $\text{TbTe}_3$ ,” *Science* **321**, 1649 (2008).
- 3 U. Bovensiepen and P. S. Kirchmann, “Elementary relaxation processes investigated by femtosecond photoelectron spectroscopy of two-dimensional materials,” *Laser Photonics Rev.* **6**, 589 (2012).

- 4 C. L. Smallwood, R. A. Kaindl, and A. Lanzara, “Ultrafast angle-resolved photoemission spectroscopy of quantum materials,” *Europhys. Lett.* **115**, 27001 (2016).
- 5 S. Aeschlimann, A. Rossi, M. Chávez-Cervantes, R. Krause, B. Arnoldi, B. Stadtmüller, M. Aeschlimann, S. Forti, F. Fabbri, C. Coletti, and J. Gierz, “Direct evidence for efficient ultrafast charge separation in epitaxial  $\text{WS}_2$ /graphene heterostructures,” *Sci. Adv.* **6**, eaay0761 (2020).
- 6 E. J. Sie, C. M. Nyby, C. D. Pemmaraju, S. J. Park, X. Shen, J. Yang, M. C. Hoffmann, B. K. Ofori-Okai, R. Li, A. H. Reid, S. Weathersby, E. Mannebach, N. Finney, D. Rhodes, D. Chenet, A. Antony, L. Balicas, J. Hone, T. P. Devereaux, T. F. Heinz, X. Wang, and A. M. Lindenberg, “An ultrafast symmetry switch in a Weyl semimetal,” *Nature* **565**, 61 (2019).
- 7 M. Dendzik, R. P. Xian, E. Peretto, D. Sangalli, D. Kutnyakhov, S. Dong, S. Beaulieu, T. Pincelli, F. Pressacco, D. Curcio, S. Y. Agustsson, M. Heber, J. Hauer, W. Wurth, G. Brenner, Y. Acremann, P. Hofmann, M. Wolf, A. Marini, G. Stefanucci, L. Rettig, and R. Ernstorfer, “Observation of an excitonic Mott transition through ultrafast core-cum-conduction photoemission spectroscopy,” *Phys. Rev. Lett.* **125**, 096401 (2020).
- 8 S. Beaulieu, S. Dong, N. Tancogne-Dejean, M. Dendzik, T. Pincelli, J. Maklar, R. P. Xian, M. A. Sentef, M. Wolf, A. Rubio, L. Rettig, and R. Ernstorfer, “Ultrafast light-induced Lifshitz transition,” *arXiv: 2003.04059* (2020).
- 9 F. Pressacco, D. Sangalli, V. Uhlir, D. Kutnyakhov, J. Ander Arregi, S. Y. Agustsson, G. Brenner, H. Redlin, M. Heber, D. Vasilyev, J. Demsar, G. Schönhense, M. Gatti, A. Marini, W. Wurth, and F. Sirotti, “Subpicosecond metamagnetic phase transition driven by non-equilibrium electron dynamics” *arXiv:2102.09265v1* (2021).
- 10 S. Hellmann, C. Sohr, M. Beye, T. Rohwer, F. Sorgenfrei, M. Marczyński-Bühlow, M. Kalläne, H. Redlin, F. Hennies, M. Bauer, A. Föhlisch, L. Kipp, W. Wurth, and K. Rossnagel, “Time-resolved x-ray photoelectron spectroscopy at FLASH,” *New J. Phys.* **14**, 013062 (2012).
- 11 A. Pietzsch, A. Föhlisch, M. Beye, M. Deppe, F. Hennies, M. Nagasono, E. Suljoti, W. Wurth, C. Gahl, and K. Döbrich, “Toward time resolved core level photoelectron spectroscopy with femtosecond x-ray free-electron lasers,” *New J. Phys.* **10**, 033004 (2008).
- 12 L.-P. Oloff, M. Oura, K. Rossnagel, A. Chainani, M. Matsunami, R. Eguchi, T. Kiss, Y. Nakatani, T. Yamaguchi, J. Miyawaki, M. Taguchi, K. Yamagami, T. Togashi, T. Katayama, K. Ogawa, M. Yabashi, and T. Ishikawa, “Time-resolved HAXPES at SACLA: Probe and pump pulse-induced space-charge effects,” *New J. Phys.* **16**, 123045 (2014).
- 13 S. Gerber, S.-L. Yang, D. Zhu, H. Soifer, J. A. Sobota, S. Rebec, J. J. Lee, T. Jia, B. Moritz, C. Jia, A. Gauthier, Y. Li, D. Leuenberger, Y. Zhang, L. Chaix, W. Li, H. Jang, J.-S. Lee, M. Yi, G. L. Dakovski, S. Song, J. M. Glowina, S. Nelson, K. W. Kim, Y.-D. Chuang, Z. Hussain, R. G. Moore, T. P. Devereaux, W.-S. Lee, P. S. Kirchmann, and Z.-X. Shen, “Femtosecond electron-phonon lock-in by photoemission and x-ray free-electron laser,” *Science* **357**, 71 (2017).
- 14 M. Greif, L. Kasmi, L. Castiglioni, M. Lucchini, L. Gallmann, U. Keller, J. Osterwalder, and M. Hengsberger, “Access to phases of coherent phonon excitations by femtosecond ultraviolet photoelectron diffraction,” *Phys. Rev. B* **94**, 054309 (2016).
- 15 G. Mercurio, I. A. Makhotkin, I. Milov, Y. Y. Kim, I. A. Zaluzhnyy, S. Dziarzhytski, L. Wenthaus, I. A. Vartanyants, and W. Wurth, “Surface structure determination by x-ray standing waves at a free electron laser,” *New J. Phys.* **21**, 033031 (2019).
- 16 D. Curcio, K. Volckaert, D. Kutnyakhov, M. Bianchi, J. Miwa, C. Sanders, S. Ulstrup, M. Heber, F. Pressacco, G. Brenner, S. Agustsson, K. Bühlmann, Y. Acremann, J. Mi, M. Bremholm, J. Demsar, W. Wurth, and P. Hofmann, “Imaging of coherent phonons in  $\text{Bi}_2\text{Se}_3$  probed by time-resolved photoelectron diffraction” (unpublished).
- 17 D. Kutnyakhov, P. Xian, M. Heber, F. Pressacco, G. Mercurio, A. Benz, G. Wenthaus, H. Meyer, S. Gieschen, K. Bühlmann, S. Däster, R. Gort, D. Curcio, K. Volckaert, M. Bianchi, Ch. Sanders, J. Miwa, S. Ulstrup, A. Oelsner, C. Tusche, Y. J. Chen, S. Y. Agustsson, D. Vasilyev, K. Medjanik, G. Brenner, S. Dziarzhytski, H. Redlin, J. Hauer, M. Dendzik, S. Dong, L. Rettig, J. Demsar, H. J. Elmers, Ph. Hofmann, R. Ernstorfer, G. Schönhense, Y. Acremann, and W. Wurth, “Time- and momentum-resolved photoemission studies using time-of-flight momentum microscopy at a free-electron laser,” *Rev. Sci. Instrum.* **91**, 013109 (2020).



- <sup>18</sup>R. P. Xian, D. Kutnyakhov, L. Rettig, Y. Acremann, F. Pressacco, S. Y. Agustsson, D. Curcio, M. Dendzik, G. Brenner, H. Redlin, M. Heber, G. Mercurio, S. Dong, J. Hauer, J. Demsar, W. Wurth, P. Hofmann, M. Scheidgen, and R. Ernstorf (2019). "Multidimensional photoemission spectra of tungsten diselenide," Zenodo. <https://doi.org/10.5281/zenodo.2704788>.
- <sup>19</sup>M. Scholz, K. Baumgärtner, C. Metzger, D. Kutnyakhov, M. Heber, C. H. Min, T. R. F. Peixoto, M. Reiser, C. Kim, W. Lu, R. Shayduk, W. M. Izquierdo, G. Brenner, F. Roth, F. Pressacco, A. Schöll, S. Molodtsov, W. Wurth, F. Reinert, and A. Madsen, "Ultrafast molecular orbital imaging of a pentacene thin film using a free electron laser," *arXiv:1907.10434* (2019).
- <sup>20</sup>F. Haag, T. Eul, P. Thielen, N. Haag, B. Stadtmüller, and M. Aeschlimann, "Time-resolved two-photon momentum microscopy—A new approach to study hot carrier lifetimes in momentum space," *Rev. Sci. Instrum.* **90**, 103104 (2019).
- <sup>21</sup>M. Keunecke, C. Möller, D. Schmitt, H. Nolte, G. S. M. Jansen, M. Reutzel, M. Gutberlet, G. Halasi, D. Steil, S. Steil, and S. Mathias, "Time-resolved momentum microscopy with a 1 MHz high-harmonic extreme ultraviolet beamline," *Rev. Sci. Instrum.* **91**, 063905 (2020).
- <sup>22</sup>J. Madéo, M. K. L. Man, C. Sahoo, M. Campbell, V. Pareek, E. L. Wong, A. Al-Mahboob, N. S. Chan, A. Karmakar, B. M. K. Mariserla, X. Li, T. F. Heinz, T. Cao, and K. M. Dani, "Directly visualizing the momentum forbidden dark excitons and their dynamics in atomically thin semiconductors," *Science* **370**, 1199–1204 (2020).
- <sup>23</sup>R. Wallauer, R. Perea-Causin, L. Münster, S. Zajusch, S. Brem, J. Güdde, K. Tanimura, K. Lin, R. Huber, E. Malic, and U. Höfer, "Direct observation of ultrafast dark exciton formation in monolayer WS<sub>2</sub>," *arXiv:2012.11385* (2020).
- <sup>24</sup>J. Bakalis *et al.*, "Time-resolved ARPES at 88 MHz repetition rate with full 2 $\pi$  electron collection" (unpublished).
- <sup>25</sup>G. S. M. Jansen, M. Keunecke, M. Düvel, C. Möller, D. Schmitt, W. Bennecke, F. J. S. Kappert, D. Steil, D. R. Luke, S. Steil, and S. Mathias, "Sparsity-driven reconstruction of molecular orbitals from angle-resolved photoemission spectroscopy," *arXiv:2001.10918* (2020).
- <sup>26</sup>R. Wallauer, M. Rath, K. Stallberg, L. Münster, D. Brandstetter, X. Yang, J. Güdde, P. Puschnig, S. Soubatch, C. Kumpf, F. C. Bocquet, F. S. Tautz, and U. Höfer, "Tracing orbital images on ultrafast time scales," *Science* **371**, 1056 (2021).
- <sup>27</sup>S. Beaulieu, J. Schusser, S. Dong, M. Schüler, T. Pincelli, M. Dendzik, J. Maklar, A. Neef, H. Ebert, K. Hricovini, M. Wolf, J. Braun, L. Rettig, J. Minár, and R. Ernstorf, "Revealing hidden orbital pseudospin texture with time-reversal dichroism in photoelectron angular distributions," *Phys. Rev. Lett.* **125**, 216404 (2020).
- <sup>28</sup>M. Keunecke, M. Reutzel, D. Schmitt, A. Osterkorn, T. A. Mishra, C. Möller, W. Bennecke, G. S. M. Jansen, D. Steil, S. R. Manmana, S. Steil, S. Kehrein, and S. Mathias, "Electromagnetic dressing of the electron energy spectrum of Au(111) at high momenta," *Phys. Rev. B* **102**, 161403(R) (2020).
- <sup>29</sup>O. Fedchenko, A. Winkelmann, K. Medjanik, S. Babenkov, D. Vasilyev, S. Chernov, C. Schlueter, A. Gloskovskii, Y. Matveyev, W. Drube, B. Schönhense, H. J. Elmers, and G. Schönhense, "High-resolution hard-x-ray photoelectron diffraction in a momentum microscope—The model case of graphite," *New J. Phys.* **21**, 113031 (2019).
- <sup>30</sup>O. Fedchenko, A. Winkelmann, S. Chernov, K. Medjanik, S. Babenkov, S. Y. Agustsson, D. Vasilyev, M. Hoesch, H.-J. Elmers, and G. Schönhense, "Emitter-site specificity of hard x-ray photoelectron Kikuchi-diffraction," *New J. Phys.* **22**, 103002 (2020).
- <sup>31</sup>K. Medjanik, O. Fedchenko, O. Yastrubchak, J. Sadowski, M. Sawicki, L. Gluba, D. Vasilyev, S. Babenkov, S. Chernov, A. Winkelmann, H. J. Elmers, and G. Schönhense, "Site-specific atomic order and band structure tailoring in the diluted magnetic semiconductor (In, Ga, Mn)As," *Phys. Rev. B* **103**, 075107 (2021).
- <sup>32</sup>X. J. Zhou, B. Wannberg, W. L. Yang, V. Brouet, Z. Sun, J. F. Douglas, D. Dessau, Z. Hussain, and Z.-X. Shen, "Space charge effect and mirror charge effect in photoemission spectroscopy," *J. Electron Spectrosc. Relat. Phenom.* **142**, 27–38 (2005).
- <sup>33</sup>G. Schiwietz, D. Kühn, A. Föhlisch, K. Holldack, T. Kachel, and N. Pontius, "Laser-pump/x-ray-probe experiments with electrons ejected from a Cu(111) target: Space-charge acceleration," *J. Synchrotron Radiat.* **23**, 1158–1170 (2016).
- <sup>34</sup>A. Verna, G. Greco, V. Lollobrigida, F. Offi, and G. Stefani, "Space-charge effects in high-energy photoemission," *J. Electron Spectrosc. Relat. Phenom.* **209**, 14–25 (2016).
- <sup>35</sup>A. Verna, G. Stefani, F. Offi, T. Gejo, Y. Tanaka, K. Tanaka, T. Nishie, K. Nagaya, A. Niozu, R. Yamamura, T. Suenaga, O. Takahashi, H. Fujise, T. Togashi, M. Yabashi, and M. Oura, "Photoemission from the gas phase using soft x-ray fs pulses: An investigation of the space-charge effects," *New J. Phys.* **22**, 123029 (2020).
- <sup>36</sup>S. Hellmann, T. Ott, L. Kipp, and K. Rossnagel, "Vacuum space-charge effects in nano-ARPES," *Phys. Rev. B* **85**, 075109 (2012).
- <sup>37</sup>L.-P. Oloff, K. Hanff, A. Stange, G. Rohde, F. Diekmann, M. Bauer, and K. Rossnagel, "Pump laser-induced space-charge effects in HHG-driven time- and angle-resolved photoelectron spectroscopy," *J. Appl. Phys.* **119**, 225106 (2016).
- <sup>38</sup>S. Ulstrup, J. C. Johannsen, F. Cilento, A. Crepaldi, J. A. Miwa, M. Zacchigna, C. Cacho, R. T. Chapman, E. Springate, F. Fromm, C. Raidel, T. Seyller, P. D. C. King, F. Parmigiani, M. Grioni, and P. Hofmann, "Ramifications of optical pumping on the interpretation of time-resolved photoemission experiments on graphene," *J. Electron Spectrosc. Relat. Phenom.* **200**, 340–346 (2015).
- <sup>39</sup>R. Al-Obaidi, M. Wilke, M. Borgwardt, J. Metje, A. Moguilevski, N. Engel, D. Tolkendorf, A. Raheem, T. Kampen, S. Mähl, I. Y. Kiyani, and E. F. Aziz, "Ultrafast photoelectron spectroscopy of solutions: Space-charge effect," *New J. Phys.* **17**, 093016 (2015).
- <sup>40</sup>C. Corder, P. Zhao, J. Bakalis, X. Li, M. D. Kershish, A. R. Muraca, M. G. White, and T. K. Allison, "Ultrafast extreme ultraviolet photoemission without space charge," *Struct. Dyn.* **5**, 054301 (2018).
- <sup>41</sup>M. Cinchetti, A. Oelsner, G. H. Fecher, H. J. Elmers, and G. Schönhense, "Observation of Cu surface inhomogeneities by multiphoton photoemission spectromicroscopy," *Appl. Phys. Lett.* **83**, 1503 (2003).
- <sup>42</sup>G. Schönhense, K. Medjanik, C. Tusche, M. de Loos, B. van der Geer, M. Scholz, F. Hieke, N. Gerken, J. Kirschner, and W. Wurth, "Correction of the deterministic part of space-charge interaction in momentum microscopy of charged particles," *Ultramicroscopy* **159**, 488 (2015).
- <sup>43</sup>E. Bauer, "Photoelectron spectromicroscopy: Present and future," *J. Electron Spectrosc. Relat. Phenom.* **114–116**, 975–987 (2001).
- <sup>44</sup>L. H. Veneklasen, "The continuing development of low-energy electron microscopy for characterizing surfaces," *Rev. Sci. Instrum.* **63**, 5513–5532 (1992).
- <sup>45</sup>C. Tusche, A. Krasnyuk, and J. Kirschner, "Spin resolved bandstructure imaging with a high resolution momentum microscope," *Ultramicroscopy* **159**, 520 (2015).
- <sup>46</sup>G. Schönhense, S. Babenkov, D. Vasilyev, H.-J. Elmers, and K. Medjanik, "Single-hemisphere photoelectron momentum microscope with time-of-flight recording," *Rev. Sci. Instrum.* **91**, 123110 (2020).
- <sup>47</sup>G. Schönhense, K. Medjanik, and H.-J. Elmers, "Space-, time- and spin-resolved photoemission," *J. Electron Spectrosc. Relat. Phenom.* **200**, 94 (2015).
- <sup>48</sup>B. Schönhense, K. Medjanik, O. Fedchenko, S. Chernov, M. Ellguth, D. Vasilyev, A. Oelsner, J. Viehhaus, D. Kutnyakhov, W. Wurth, H. J. Elmers, and G. Schönhense, "Multidimensional photoemission spectroscopy—The space-charge limit," *New J. Phys.* **20**, 033004 (2018).
- <sup>49</sup>K. Rossnagel, "Pushing the space-charge limit in electron momentum microscopy," *New J. Phys.* **20**, 021001 (2018).
- <sup>50</sup>P. W. Hawkes and E. Kasper, *Principles of Electron Optics* (Academic Press, 1996).
- <sup>51</sup>H. Seiler, "Secondary electron emission in the scanning electron microscope," *J. Appl. Phys.* **54**, R1–R18 (1983).
- <sup>52</sup>O. Schmidt, G. H. Fecher, Y. Hwu, and G. Schönhense, "The spatial distribution of non-linear effects in sub-threshold photoemission from metallic adsorbates on Si(111)," *Surf. Sci.* **482–485**, 687 (2001).
- <sup>53</sup>O. Schmidt, M. Bauer, C. Wiemann, R. Porath, M. Scharfe, O. Andreyev, G. Schönhense, and M. Aeschlimann, "Time-resolved two photon photoemission electron microscopy," *Appl. Phys. B* **74**, 223 (2002).
- <sup>54</sup>M. Cinchetti, D. A. Valdaitsev, A. Gloskovskii, A. Oelsner, S. A. Nepijko, and G. Schönhense, "Photoemission time-of-flight spectromicroscopy of Ag nanoparticle films on Si(111)," *J. Electron. Spectrosc. Rel. Phenom.* **137–140**, 249 (2004).
- <sup>55</sup>M. Cinchetti and G. Schönhense, "Two-photon photoemission spectromicroscopy of noble metal clusters on surfaces studied using time-of-flight photoemission electron microscopy," *J. Phys.: Condens. Matter* **17**, S1319 (2005).
- <sup>56</sup>A. Gloskovskii, D. A. Valdaitsev, M. Cinchetti, S. A. Nepijko, J. Lange, M. Aeschlimann, M. Bauer, M. Klimenkov, L. V. Viduta, P. M. Tomchuk, and

- G. Schönhense, "Electron emission from films of Ag and Au nanoparticles excited by a femtosecond pump-probe laser," *Phys. Rev. B* **77**, 195427 (2008).
- <sup>57</sup>M. Cinchetti, A. Gloskovskii, S. A. Nepjiko, G. Schönhense, H. Rochholz, and M. Kreiter, "Photoemission electron microscopy as a tool for the investigation of optical near fields," *Phys. Rev. Lett.* **95**, 047601 (2005).
- <sup>58</sup>F. Schertz, M. Schmelzeisen, M. Kreiter, H.-J. Elmers, and G. Schönhense, "Field emission of electrons generated by the near field of strongly coupled plasmons," *Phys. Rev. Lett.* **108**, 237602 (2012).
- <sup>59</sup>F. Schertz, M. Schmelzeisen, R. Mohammadi, M. Kreiter, H.-J. Elmers, and G. Schönhense, "Near field of strongly coupled plasmons: Uncovering dark modes," *Nano Lett.* **12**, 1885 (2012).
- <sup>60</sup>M. Lehr, B. Foerster, M. Schmitt, K. Krüger, C. Sönnichsen, G. Schönhense, and H.-J. Elmers, "Momentum distribution of electrons emitted from resonantly excited individual gold nanorods," *Nano Lett.* **17**, 6606 (2017).
- <sup>61</sup>R. P. Xian, Y. Acremann, S. Y. Agustsson, M. Dendzik, K. Bühlmann, D. Curcio, D. Kutnyakhov, F. Pressacco, M. Heber, S. Dong, T. Pincelli, J. Demsar, W. Wurth, P. Hofmann, M. Wolf, M. Scheiden, L. Rettig, and R. Ernstorfer, "An open-source, end-to-end workflow for multidimensional photoemission spectroscopy," *Sci. Data* **7**, 442 (2020).
- <sup>62</sup>J. Graf, S. Hellmann, C. Jozwiak, C. L. Smallwood, Z. Hussain, R. A. Kaindl, L. Kipp, K. Rossnagel, and A. Lanzara, "Vacuum space charge effect in laser-based solid-state photoemission spectroscopy," *J. Appl. Phys.* **107**, 014912 (2010).
- <sup>63</sup>J. Maklar, S. Dong, S. Beaulieu, T. Pincelli, M. Dendzik, Y. W. Windsor, R. P. Xian, M. Wolf, R. Ernstorfer, and L. Rettig, "A quantitative comparison of time-of-flight momentum microscopes and hemispherical analyzers for time- and angle-resolved photoemission spectroscopy experiments," *Rev. Sci. Instrum.* **91**, 123112 (2020).
- <sup>64</sup>A. K. Mills, S. Zhdanovich, M. X. Na, F. Boschini, E. Razzoli, M. Michiardi, A. Sheyerman, M. Schneider, T. J. Hammond, V. Süß, C. Felser, A. Damascelli, and D. J. Jones, "Cavity-enhanced high harmonic generation for extreme ultraviolet time- and angle-resolved photoemission spectroscopy," *Rev. Sci. Instrum.* **90**, 083001 (2019).
- <sup>65</sup>A. Zhao, M. van Beuzekom, B. Bouwens, D. Byelov, I. Chakaberia, C. Cheng, E. Maddox, A. Nomerotski, P. Svihra, J. Visser, V. Vrba, and T. Weinacht, "Coincidence velocity map imaging using Tpx3Cam, a time stamping optical camera with 1.5 ns timing resolution," *Rev. Sci. Instrum.* **88**, 113104 (2017).
- <sup>66</sup>G. Giacomini, W. Chen, F. Lanni, and A. Tricoli, "Development of a technology for the fabrication of low-gain avalanche diodes at BNL," *Nucl. Instrum. Methods Phys. Res., Sect. B* **934**, 52 (2019).
- <sup>67</sup>See <https://www.surface-concept.com/index.html> and [https://www.surface-concept.com/downloads/info/ml\\_dld.pdf](https://www.surface-concept.com/downloads/info/ml_dld.pdf) for multiline detectors.
- <sup>68</sup>H. Matsuda, L. Tóth, F. Matsui, and H. Daimon, "Evaluation of disturbing effect of mesh holes in wide-acceptance-angle electrostatic mesh lenses," *J. Electron Spectrosc. Relat. Phenom.* **195**, 78–84 (2014).
- <sup>69</sup>G. Schönhense, O. Fedchenko, K. Medjanik, S. Babenkov, D. Vasilyev, and H. J. Elmers, "Asymmetric dodecapole: an imaging bandpass filter for photoelectron momentum microscopes" (unpublished).
- <sup>70</sup>J. D. Jackson, *Classical Electrodynamics*, 3rd ed. (Wiley, 1998), ISBN: 9780471309321.
- <sup>71</sup>N. D. Lang and W. Kohn, "Theory of metal surfaces: Work function," *Phys. Rev. B* **3**, 1215–1223 (1970).
- <sup>72</sup>D. Cahen and A. Kahn, "Electron energetics at surfaces and interfaces: Concepts and experiments," *Adv. Mater.* **15**, 271 (2003).
- <sup>73</sup>G. W. Parker, "Electric field outside a parallel plate capacitor," *Am. J. Phys.* **70**, 502 (2002).
- <sup>74</sup>K. Medjanik, S. V. Babenkov, S. Chernov, D. Vasilyev, B. Schönhense, C. Schlueter, A. Gloskovskii, Y. Matveyev, W. Drube, H. J. Elmers, and G. Schönhense, "Progress in HAXPES performance combining full-field k-imaging with time-of-flight recording," *J. Synchrotron Radiat.* **26**, 1996–2012 (2019).
- <sup>75</sup>K. Medjanik, O. Fedchenko, S. Chernov, D. Kutnyakhov, M. Ellguth, A. Oelsner, B. Schönhense, T. R. F. Peixoto, P. Lutz, C.-H. Min, F. Reinert, S. Däster, Y. Acremann, J. Viefhaus, W. Wurth, H. J. Elmers, and G. Schönhense, "Direct 3D mapping of the Fermi surface and Fermi velocity," *Nat. Mater.* **16**, 615 (2017).
- <sup>76</sup>G. Schönhense and B. Schönhense, "Device for the reduction of space-charge interaction in electron-spectroscopic instruments," German patent DE10 2017 126 882 B3 (January 2019).
- <sup>77</sup>D. A. Dahl, T. R. McJunkin, and J. R. Scott, "Comparison of ion trajectories in vacuum and viscous environments using SIMION: Insights for instrument design," *Int. J. Mass Spectrom.* **266**, 156–165 (2007), <http://www.sisweb.com>, primary author: David J. Manura, SIS (version 8.1/8.0/SL).
- <sup>78</sup>M. Martins *et al.*, "Monochromator beamline for FLASH," *Rev. Sci. Instrum.* **77**, 115108 (2006).
- <sup>79</sup>N. Gerasimova, S. Dziarzhytski, and J. Feldhaus, "The monochromator beamline at FLASH: Performance, capabilities and upgrade plans," *J. Mod. Opt.* **58**, 1480–1485 (2011).
- <sup>80</sup>L. Miaja-Avila, C. Lei, M. Aeschlimann, J. L. Gland, M. M. Murnane, H. C. Kapteyn, and G. Saathoff, "Laser-assisted photoelectric effect from surfaces," *Phys. Rev. Lett.* **97**, 113604 (2006).
- <sup>81</sup>G. Saathoff, L. Miaja-Avila, M. Aeschlimann, M. M. Murnane, and H. C. Kapteyn, "Laser-assisted photo-emission from surfaces," *Phys. Rev. A* **77**, 022903 (2008).
- <sup>82</sup>D. Kutnyakhov, S. Chernov, K. Medjanik, R. Wallauer, C. Tusche, M. Ellguth, S. A. Nepjiko, M. Krivenkov, J. Braun, S. Borek, J. Minar, H. Ebert, H. J. Elmers, and G. Schönhense, "Spin texture of time-reversal symmetry invariant surface states on W(110)," *J. Phys.: Condens. Matter* **6**, 29394 (2016).
- <sup>83</sup>M. Reutzel, A. Li, and H. Petek, "Coherent two-dimensional multiphoton photoelectron spectroscopy of metal surfaces," *Phys. Rev. X* **9**, 011044 (2019).
- <sup>84</sup>A. Li, N. A. James, T. Wang, Z. Wang, H. Petek, and M. Reutzel, "Toward full surface Brillouin zone mapping by coherent multi-photon photoemission," *New J. Phys.* **22**, 073035 (2020).
- <sup>85</sup>*Hard X-Ray Photoelectron Spectroscopy (HAXPES)*, Springer Series in Surface Sciences Vol. 59, edited by J. C. Woicik (Springer, 2016), pp. 141–157.
- <sup>86</sup>C. Kalha *et al.*, "Hard X-ray photoelectron spectroscopy: A snapshot of the state-of-the-art in 2020," *J. Phys.: Condens. Matter* (2021).
- <sup>87</sup>S. Babenkov, K. Medjanik, D. Vasilyev, S. Chernov, C. Schlueter, A. Gloskovskii, Yu. Matveyev, W. Drube, B. Schönhense, K. Rossnagel, H.-J. Elmers, and G. Schönhense, "High-accuracy bulk electronic bandmapping with eliminated diffraction effects using hard X-ray photoelectron momentum microscopy," *Commun. Phys.* **2**, 107 (2019).
- <sup>88</sup>H. J. Elmers, S. V. Chernov, S. W. D'Souza, S. P. Bommanaboyena, S. Yu. Bodnar, K. Medjanik, S. Babenkov, O. Fedchenko, D. Vasilyev, S. Y. Agustsson, C. Schlueter, A. Gloskovskii, Yu. Matveyev, V. N. Strocov, Y. Skourski, L. Šmejkal, J. Sinova, J. Minár, M. Kläui, G. Schönhense, and M. Jourdan, "Néel vector induced manipulation of valence states in the collinear antiferromagnet Mn<sub>2</sub>Au," *ACS Nano* **14**, 17554–17564 (2020).
- <sup>89</sup>G. Schönhense, K. Medjanik, S. Babenkov, D. Vasilyev, M. Ellguth, O. Fedchenko, S. Chernov, B. Schönhense, and H.-J. Elmers, "Momentum-transfer model of valence-band photoelectron diffraction," *Commun. Phys.* **3**, 45 (2020).
- <sup>90</sup>H.-J. Elmers, J. Regel, T. Mashof, J. Braun, S. Babenkov, S. Chernov, O. Fedchenko, K. Medjanik, D. Vasilyev, J. Minar, H. Ebert, and G. Schönhense, "Rashba splitting of the Tamm surface state on Re(0001) observed by spin-resolved photo-emission and scanning tunnelling spectroscopy," *Phys. Rev. Res.* **2**, 013296 (2020).
- <sup>91</sup>C. Schlueter, A. Gloskovskii, K. Ederer, I. Schostak, S. Piec, I. Sarkar, Yu. Matveyev, P. Lömker, M. Sing, R. Claessen, C. Wiemann, C. M. Schneider, K. Medjanik, G. Schönhense, P. Amann, A. Nilsson, and W. Drube, "The new dedicated HAXPES beamline P22 at PETRAIII," *AIP Conf. Proc.* **2054**, 040010 (2019).
- <sup>92</sup>T. Konstantinova *et al.*, "Nonequilibrium electron and lattice dynamics of strongly correlated Bi<sub>2</sub>Sr<sub>2</sub>CaCu<sub>2</sub>O<sub>8+δ</sub> single crystals," *Sci. Adv.* **4**, 7427 (2018).
- <sup>93</sup>P. Beaud, A. Caviezel, S. O. Mariager, L. Rettig, G. Ingold, C. Dornes, S.-W. Huang, J. A. Johnson, M. Radovic, T. Huber, T. Kubacka, A. Ferrer, H. T. Lemke, M. Chollet, D. Zhu, J. M. Glowia, M. Sikorski, A. Robert, H. Wadati, M. Nakamura, M. Kawasaki, Y. Tokura, S. L. Johnson, and U. Staub, "A time-dependent order parameter for ultrafast photoinduced phase transitions," *Nat. Mater.* **13**, 923 (2014).